The Dissertation Committee for Sunghwan Yi
certifies that this is the approved version of the following dissertation:

Injection in Plasma-Based Electron Accelerators

Committee:

Gennady Shvets, Supervisor

Mike Downer

Herbert Berk

Wendell Horton, Jr.

Pawan Kumar

Injection in Plasma-Based Electron Accelerators

by

Sunghwan Yi, B.S.

DISSERTATION

Presented to the Faculty of the Graduate School of

The University of Texas at Austin

in Partial Fulfillment

of the Requirements

for the Degree of

DOCTOR OF PHILOSOPHY

THE UNIVERSITY OF TEXAS AT AUSTIN

December 2012

Acknowledgments

This thesis represents the work of many scientists. Most importantly, I must thank my advisor Professor Gennady Shvets for guiding this research, in addition to laboring tirelessly to secure the funding which made this work possible. I also wish to thank Drs. Vladimir Khudik and Serguei Kalmykov who provided me with hands on training and with whom I collaborated closely in my daily research. Furthermore, the theoretical research presented here has benefited in many ways from a productive collaboration with the experimental group of Professor Mike Downer, including Drs. Xiaoming Wang and Steve Reed, with whom I had many useful discussions. I must also thank the members of my dissertation committee for their feedback which made this thesis possible. Funding for this work was provided by the US Department of Energy and the University of Texas Physics Department. Supercomputing resources were provided by the Texas Advanced Computing Center.

Injection in Plasma-Based Electron Accelerators

Publication No. _____

Sunghwan Yi, Ph.D.
The University of Texas at Austin, 2012

Supervisor: Gennady Shvets

Plasma-based accelerators aim to efficiently generate relativistic electrons by exciting plasma waves using a laser or particle beam driver, and "surfing" electrons on the resulting wakefields. In the blowout regime of such wakefield acceleration techniques, the intense laser radiation pressure or beam fields expel all of the plasma electrons transversely, forming a region completely devoid of electrons ("bubble") that co-propagates behind the driver. Injection, where initially quiescent background plasma electrons become trapped inside of the plasma bubble, can be caused by a variety of mechanisms such as bubble expansion, field ionization or collision between pump and injector pulses. This work will present a study of the injection phenomenon through analytic modeling and particle-in-cell (PIC) simulations. First, an idealized model of a slowly expanding spherical bubble propagating at relativistic speeds is used to demonstrate the importance of the bubble's structural dynamics in self-injection. This physical picture of injection is verified though a reduced PIC approach which makes possible the modeling of problem sizes intractable to

first-principles codes. A more realistic analytic model which takes into account the effects of the detailed structure of the fields surrounding the bubble in the injection process is also derived. Bubble expansion rates sufficient to cause injection are characterized. A new mechanism for generation of quasi-monoenergetic electron beams through field ionization induced injection is presented, and simulation results are compared to recent experimental results. Finally, a technique for frequency-domain holographic imaging of the evolving bubble is analyzed using PIC as well as a novel simulation method for laser probe beam propagation.

Table of Contents

Chapter 1

Introduction

1.1 Plasma-based accelerators

Plasma-based accelerators aim to efficiently generate electrons with relativistic energies by exciting plasma density oscillations and utilizing the resultant fields as a dynamically produced accelerating structure. These electron density oscillations, i.e. Langmuir waves [1], are driven by either the radiation pressure of an intense laser pulse or the electromagnetic fields of a relativistic charged particle beam, and as such these waves have a phase velocity close to the speed of light $v_{\mathrm{ph}} \sim c$. Electrons that become synchronous with the accelerating phase of the plasma wave gain energy at the expense of the wave energy. Thus, this technology uses the plasma as a medium to transfer energy from a laser pulse or particle beam driver to an electron beam.

The concept of the plasma-based accelerator was first proposed by Tajima and Dawson in their seminal paper of 1979 [2], and in the past decade this technique has been proven in the laboratory to create monoenergetic electron beams of the order 1 GeV [3, 4, 5, 6, 7]. When non-monoenergetic beams are taken into account, maximum electron energies on the order of 10 GeV [8] have also been achieved. As the technology matures, more energetic, higher

charge and better quality (narrow energy spread and low divergence) electron beams are expected to become available. These accelerators will thus have applications such as the generation of x-rays for materials and biological research [9], colliders for high energy physics research [10, 11], and radiation therapy in oncology [12, 13].

The primary advantage of plasma-based acceleration is the larger amplitude fields supported by plasmas compared to that found in conventional radio frequency accelerating structures. In an RF accelerator, the maximum achievable field is limited by breakdown or arcing in the high voltage vacuum cavity. With current technology, this limits the accelerating gradient in an RF accelerator to ~ 100 MV/m. In a plasma-based scheme the accelerating cavity is not in vacuum, but instead filled with an already broken down plasma and hence not subject to disruption of the fields by arcing. Indeed, the Langmuir waves excited in a plasma-based accelerator support electric fields on the order of $E_\parallel = m_e c \omega_p / e$ where m_e is the electron mass, c is the speed of light, e is the electron charge and $\omega_p = (4\pi e^2 n_0 / m_e)^{1/2}$ is the plasma frequency, or

$$E_\parallel (\mathrm{V/cm}) \sim \sqrt{n_0 (\mathrm{cm}^{-3})}\,, \tag{1.1}$$

where n_0 is the background plasma electron density. For a typical density of $n_0 = 10^{18}$ cm^{-3} the accelerating field is $E_\parallel \sim 100$ GV/m, about three orders or magnitude greater than the maximum fields in an RF accelerator. With such an improvement in acceleration efficiency, it is possible to envision a major reduction in the size and cost of electron acceleration facilities.

1.2 History of plasma based accelerators

There have been several plasma based acceleration schemes of historical interest, which have evolved as available laser and beam drivers have improved. The laser wakefield accelerator (LWFA) concept as first proposed [2] called for the resonant excitation of a plasma wave by a single high-intensity ($I \gtrsim 10^{17}$ W/cm^2) laser pulse of length $\tau_L \sim \lambda_p$, where $\lambda_p \equiv 2\pi c/\omega_p$ is the plasma wavelength. For typical laboratory plasma densities this required the use of sub-picosecond laser pulse drivers, a technology that was unavailable until the advent of chirped-pulse amplification in 1988 [14]. To address this issue the plasma beatwave accelerator (PBWA) [2, 15] was proposed.

In the PBWA scheme two laser pulses are employed that are detuned in frequency by $\Delta\omega \sim \omega_p$. The pulses are not required in this case to be shorter than the plasma wavelength, since the excitation of the plasma wave is due to the ponderomotive force of the laser beatwave. Rather, each beat in the beatwave has a duration of ω_p, satisfying the resonance condition. The generation of plasma waves by a laser beatwave was first demonstrated experimentally in 1985 [16] and electron acceleration was successfully observed in the early 1990s [17, 18]. These early experiments achieved electron energies on the order of 10 MeV by beating two lines of a CO_2 laser.

The self-modulated laser wakefield accelerator [19, 20] (SM-LWFA) similarly takes advantage of a train of laser pulses that resonantly excite a Langmuir wave. In contrast to the PBWA, however, the pulse train is produced from a single long pulse by the self-modulation instability. In the self-modulation in-

stability the co-propagating plasma wave initially generated by the long pulse acts as a periodic focusing and defocusing optic depending on the density wave phase. As seen from Eq. (1.9), regions of lower density focus the laser intensity while regions of higher density defocus, owing to the opposite signs of the radial density gradient in the different phases. The ponderomotive force of the laser driver is thus enhanced in the low density regions and suppressed in the high density ones, causing a nonlinear feedback which causes the instability to grow. The result is the longitudinal break up of the long laser pulse into a train of short pulses that resonantly excite a large amplitude plasma wave.

Since the SM-LWFA is not limited to plasma densities that are initially resonant with the laser pulse duration, it is possible to operate a SM-LWFA at a higher density than would be possible with LWFA. This is advantageous since the threshold laser power required for relativistic self-focusing given by [21]

$$P_c = 17 \text{ GW } \left(\frac{\omega_0}{\omega_p}\right)^2 , \tag{1.2}$$

decreases with increasing density. Thus, by operating at a higher density a SM-LWFA extends the acceleration length due to suppression of the laser diffraction by the relativistic self-focusing effect. However, the density cannot be increased indefinitely, since at higher densities the dephasing between electrons undergoing acceleration and the plasma wave occurs more rapidly due to the decreased laser group velocity, limiting the acceleration length.

Excitation of plasma waves by the self-modulation instability and the associated pulse train generation was first observed experimentally in 1995 [22,

23, 24], producing electrons with energies in excess of 44 MeV. Although the SM-LWFA and the PBWA schemes for plasma based acceleration have been successful in producing relativistic electron beams, these have been of relatively broad energy spectra making them unsuitable for use in applications. An important development occurred in 2002 however, when the bubble regime was first proposed theoretically by Pukhov *et al.* [25].

In the bubble regime, the intense driver expels all electrons transversely as it travels through the plasma, creating a density cavity devoid of electrons behind it. Ions are immobile on the characteristic response time scale of the of the plasma electrons ω_p^{-1}, and remain inside the cavity. Electrons are eventually attracted back towards this ion column, and close off the bubble.

To blow out a bubble and cause complete cavitation there are more stringent requirements imposed on driver parameters compared to the previously discussed schemes. To access the highly nonlinear bubble regime, the drive pulse must be very intense; in the case of a laser driver the normalized vector potential of the focused pulse must be highly relativistic, $a_0 \gtrsim 1$, while for a beam driver the current must be high, $I \gtrsim I_A$ where $I_A \equiv mc^3/e$ is the Alfvén current. The drive pulse must also be of short duration so that $\tau_{driver} \sim \omega_p^{-1}$, in order for the driver to resonantly excite a strong plasma wave and cause blowout. A typical experimental plasma density of $n_0 \approx 10^{17}$ cm^{-3} necessitates $\tau_{driver} \sim 100$fs. Because of the requirement for intense ultrashort drivers, the bubble regime could not be attained experimentally until tightly focused laser pulses temporally compressed using the chirped-pulse amplifica-

tion technique were employed [26, 27, 28].

Despite these challenging requirements modern plasma based accelerators typically operate in the bubble regime due to the several advantages it offers. Most importantly, the first successful bubble regime experiments demonstrated the generation of quasimonoenergetic electron beams [26, 27, 28]. The higher quality of the energy spectra observed in the bubble regime makes these electron beams more suited to applications, when compared to the relatively broad or even continuous spectra observed in the previously mentioned acceleration schemes (i.e., PBWA and SM-LWFA). The bubble also supports higher peak accelerating fields than non-blownout wakes. A large enough plasma bubble can in fact have an accelerating gradient many times greater [29] than the cold nonrelativistic wave breaking field [30] given by Eq. (1.1). In addition, the bubble structure features focusing fields that increase linearly from the bubble axis [29], allowing for generation of tightly collimated electron beams. For the case of laser driven bubbles a combination of relativistic self-focusing [31, 21] and the refractive effect of the transverse density gradient (known as ponderomotive self-channeling) [32] can lead to self-guiding of the drive pulse, eliminating the need for complex external guiding structures for acceleration lengths beyond a Rayleigh length. Lastly, self-injection may occur, where initially quiescent background plasma electrons become in-phase with the bubble accelerating structure. This allows the plasma itself to act as a cathode, obviating the need for external electron injectors and avoiding the associated synchronization problems. This phenomenon of self-injection in the

bubble regime is the central topic of study in this thesis.

1.3 Drive mechanisms

Exciting high amplitude Langmuir waves requires the use of a driver that interacts strongly with the plasma. There are two major types of drivers that are used in plasma based accelerators: intense laser pulses and charged particle beams. A laser drive pulse exerts a force on the plasma through the ponderomotive force [33], a nonlinear force which causes charged particles to drift towards the lower intensity regions of an oscillating field with an inhomogeneous spacial profile. The expression for the ponderomotive force is derived by considering the equation of motion of a cold collisionless plasma given by

$$\frac{d\mathbf{p}}{dt} = -e\left(\mathbf{E} + \frac{\mathbf{v}}{c} \times \mathbf{B}\right), \tag{1.3}$$

where $\mathbf{p}$ is the electron fluid momentum and $\mathbf{v}$ is the electron fluid velocity, and the electromagnetic fields are given by

$$\mathbf{E} = -\frac{1}{c}\frac{\partial \mathbf{A}}{\partial t}, \quad \mathbf{B} = \nabla \times \mathbf{A}, \tag{1.4}$$

where $\mathbf{A}$ is the vector potential. The first-order response in the oscillating field of the laser is given by $\partial \mathbf{p}_1/\partial t = -e\mathbf{E}$, so that the quiver motion is $\mathbf{p}_1 = m_e c\mathbf{a}$ where $\mathbf{a} \equiv e\mathbf{A}/m_e c^2$ is the normalized vector potential. The second-order motion can then be written

$$\frac{d\mathbf{p}_2}{dt} = -\frac{d\mathbf{p}_1}{dt} - m_e c\left[-\frac{\partial \mathbf{a}}{\partial t} + \frac{\mathbf{p}_1}{m_e} \times (\nabla \times \mathbf{a})\right] \tag{1.5}$$

$$= -\left(\frac{\mathbf{p}_1}{m_e} \cdot \nabla\right)\mathbf{p}_1 - c\mathbf{p}_1 \times (\nabla \times \mathbf{a}), \tag{1.6}$$

where cancellation occurs since $d\mathbf{p}_1/dt = \partial\mathbf{p}_1/\partial t + (\mathbf{v}_1 \cdot \nabla)\mathbf{p}_1$. Eliminating the quiver motion $\mathbf{p}_1$ on the right hand side of Eq. (1.6) in favor of the normalized vector potential $\mathbf{a}$ gives the desired expression for the ponderomotive force

$$\frac{d\mathbf{p}_2}{dt} = -m_e c^2 \left[(\mathbf{a} \cdot \nabla)\mathbf{a} + \mathbf{a} \times (\nabla \times \mathbf{a})\right] \tag{1.7}$$

$$= \mathbf{F}_p \equiv -\frac{m_e c^2}{2} \nabla |a|^2 \,, \tag{1.8}$$

by use of a vector identity. The ponderomotive force is thus proportional to the gradient of the electromagnetic energy density and may be thought of as a radiation pressure pushing particles in the direction of lower laser intensity.

The propagation of the laser drive pulse can be described by the standard paraxial wave theory, which is a valid approximation as long as the pulse envelope varies slowly relative to laser period and is focused to a spot size much larger than the wavelength. Solutions of the paraxial wave equation in vacuum imply that the laser diffracts within a Rayleigh length $z_R = \pi w_0^2/\lambda_0$, where w_0 is the focal spot size and λ_0 is the laser wavelength. Pump diffraction limits the acceleration length, but in plasma the diffraction may be mitigated by focusing effects of the plasma. These plasma guiding effects may be summarized by considering the plasma refractive index [34]

$$N \approx 1 - \frac{\omega_p^2}{2\omega_0^2}\left(1 - \frac{|a|^2}{2} + \frac{\delta n}{n_0}\right) \tag{1.9}$$

where ω_0 is the laser frequency and δn is the density perturbation. The expression in Eq. (1.9) is valid for modest laser intensities ($|a|^2 \ll 1$) in the limit of small amplitude density perturbations ($\delta n/n_0 \ll 1$). The term proportional

to $|a|^2$ in Eq. (1.9) represents relativistic corrections to the electron mass due to its quiver motion, and for an appropriate transverse laser profile can lead to relativistic self-focusing [31]. In fact the transverse intensity profile must simply have a maximum on axis and decrease with increasing distance from axis for relativistic self-focusing to occur. The term proportional to δn represents the refractive effect of the plasma density gradient, and in practice may include an external plasma density channel. For a plasma wave this term may be focusing or defocusing along the length of the wake, depending on the phase.

A charged particle beam may also be used as a driver for plasma based accelerators [35, 36]. In this case the maximum energy gain possible for the accelerated electrons is limited by the transformer ratio, defined as the ratio between the maximum accelerating field of the wake and the maximum decelerating field within the drive beam itself. Depending on the longitudinal density profile of the drive beam [37] the transformer ratio is a number of order one but greater than one. Thus, it is possible to drive a wakefield with an electron beam and produce accelerated electrons that have greater individual particle energies than the drive beam itself. For example, through the use of wakefield acceleration the maximum energy of a kilometers long conventional linear electron accelerator may be doubled in a meter of plasma [8]. Due to the restriction in energy gain imposed by the transformer ratio, achieving TeV electron energies of relevance to collider applications in high energy physics research is not possible using currently available electron beam drivers. It

has thus been proposed to drive plasma based accelerators with proton beam drivers from state of the art hadron collider facilities [10], to transfer the energy from TeV protons to electrons.

1.4 Summary

In brief, plasma based accelerators offer efficient generation of relativistic electron beams by taking advantage of the high fields that can be supported by plasmas. The accelerating fields are excited by driving Langmuir waves using either the ponderomotive force of an intense laser or the space charge fields of a charged particle beam. Electrons that become synchronous with the plasma wave gain energy. There have been several historical schemes for wakefield accelerators studied in the past, which strove to resonantly excite large amplitude plasma waves by generating a laser pulse train. These pulse trains were created by beating two frequency detuned laser pulses with the difference frequency matched to the plasma frequency, or self-consistently generated through the self-modulation instability between the plasma wave and a single long laser pulse. As shorter, more intense drivers became available, however, the highly nonlinear bubble regime became accessible. Modern plasma based accelerators typically operate in the bubble regime due to the large acceleration gradients and focusing fields, as well as the high spectral quality of electron beams generated. Self-injection can also occur in the bubble regime, where initially stationary plasma electrons become trapped by the relativistic bubble.

The following chapters are organized as follows: Chapter 2 is a study of electron self-injection in the context of laser driven wakefield accelerators. Using an idealized spherical model of the plasma bubble it is shown that an expanding bubble can trap electrons by acting as a dynamically deepening potential well. A trapping condition is derived and the expansion rates sufficient for trapping are characterized as a function of the phase velocity of the bubble. Chapter 3 analyzes self-injection in the context of electron beam driven wakefield accelerators. A realistic model of the beam driven bubble is derived which takes into account the detailed charge and current distribution in the regions immediately surrounding the bubble. It is shown that the associated electromagnetic fields outside the bubble determine the trapping dynamics, and critical expansion rates for trapping are characterized with respect to the bubble size. Chapter 4 studies an alternative injection mechanism to bubble expansion, which relies on field ionization of dopant gas electrons by the driver inside the bubble potential well. A method for generation of quasimonoenergetic electron beams using this injection scheme is described. The effects of driver evolution and dopant species on the electron beam quality are analyzed. Chapter 5 analyzes the application of frequency domain holographic imaging to plasma based accelerators in the bubble regime. Techniques for experimental measurement of the presence of plasma bubbles as well as their evolution are described and modeled. A summary of the results are presented in Chapter 6.

Chapter 2

Self-injection in laser driven wakefield accelerators

2.1 Laser wakefield acceleration

An important development in the field of plasma-based laser wakefield accelerators (LWFA) occurred in 2004 when the first quasi-monoenergetic electrons in the 100 MeV range were produced [26, 27, 28]. Soon afterwards, generation of GeV-scale quasi-monoenergetic electron beams from centimeter-long plasmas were demonstrated [3, 4, 5, 6, 7]. All of these experiments were carried out in the bubble regime [38, 25], demonstrating the advantage of the bubble over previous plasma based acceleration techniques.

The structure of the electromagnetic fields inside the bubble has been extensively investigated in the past, and several simplified models [29, 39] have been successfully developed. Since the bulk of the ambient plasma electrons interact briefly with the bubble and only support the bubble fields, the crucial question is how some of the plasma electrons become injected inside of the bubble. In fact, both the total charge and the quality of the resulting electron beam depends critically on the details of the self-injection process, which is the focus of this chapter. Earlier work focused on electron injec-

tion by a non-evolving bubble [29, 40] propagating through relatively dense plasmas. It has also been demonstrated [41] that dynamic expansion of the bubble drastically changes the injection process and enables electron trapping from a tenuous plasma. This chapter explores in detail electron trapping into the deepening potential well of an expanding bubble. An idealized spherical model of an evolving bubble is developed, extending previous work [29] which considered the case of a non-evolving bubble only. A sufficient condition for formal trapping inside the bubble potential well is derived, and the relationship between trapped and injected but not formally trapped electrons is analyzed. Expansion rates sufficient for trapping and acceleration are characterized as a function of the bubble velocity, which is significant for tenuous plasmas since the bubble speed is determined by the group velocity of the laser driver and hence background plasma density. The generation of high-quality ultra-relativistic electron beams by phase space rotation within an expanding bubble is analyzed. Results from the simplified model are validated using PIC simulations.

The remainder of the chapter is organized as follows. Sec. 2.2 contains a review the simplified description of the plasma bubble [29, 40] modeled as a spherical cavity devoid of plasma electrons propagating with a relativistic velocity. This model is used to gain qualitative understanding of the self-injection mechanism by the evolving bubble. The criteria for trapping are derived in Sec. 2.2.2: the minimal bubble expansion rate, and the minimum change of the electron's moving frame Hamiltonian calculated in the Galilean

reference frame of the bubble. Test-particle simulations are used to calculate the minimal bubble expansion rate required for electron trapping into the model bubble as a function of the bubble's Lorentz factor γ_0. It is shown in Sec. 2.2.3 that, for a model bubble, $\Delta H = -m_e c^2$ is a highly accurate condition for both injection and trapping when $\gamma_0 \gg k_p R$. For slower bubbles, a much smaller change of the Hamiltonian is needed for injection. The formation of monoenergetic electron beams due to phase space rotation of the electrons injected into the bubble at different times is discussed in Sec. 2.2.4.

Sec. 2.3 verifies the qualitative features of the above model for electron self-injection and trapping using the quasi-static PIC code WAKE [42]. These simulations demonstrate that temporal expansion of the bubble is the dominant mechanism of electron self-injection and trapping in rarefied plasmas. Such plasmas (i.e., $n_0 \sim 10^{17}$ cm^{-3}) are relevant to LWFA with petawatt-class lasers. It is further shown that a combination of bubble expansion and stabilization terminates the self-injection process, and together with phase space rotation results in the generation of quasi-monoenergetic electron beams. Results are summarized in Sec. 2.4.

2.2 Electron trapping and acceleration by a simplified plasma bubble

2.2.1 Description of the simplified plasma bubble

To evaluate the importance of bubble evolution for electron self-injection, we begin our analysis with a simplified model of the plasma bubble [29, 40].

The bubble is described as a sphere of radius R devoid of electrons that travels through the plasma with a relativistic velocity $\mathbf{v} = v_0\mathbf{e}_z$. A more realistic model of the bubble will be considered in Chapter 3. A modification to the spherical bubble model with a localized maximum in density near the tail of the bubble has been shown to affect the self-injection dynamics [29], and will be considered in Sec. 2.2.3.

Because the bubble trails the laser pulse, its velocity is assumed to be close to the group velocity of the laser pulse, i.e., $\gamma_0 = (1 - v_g^2)^{-1/2} = \omega_0/\omega_p$, where ω_0 is the laser frequency. For the remainder of this Section we use the normalized quantities, where time is normalized to ω_p^{-1}, length to k_p^{-1}, velocities to c, and potential to $m_e c^2/|e|$. Using the gauge $A_z + \phi = 0$ and introducing $\Phi \equiv A_z - \phi$, where $\mathbf{A}$ and ϕ are the vector and scalar potentials, it can be shown [29] that the potential inside the bubble is

$$\Phi(\rho \leq R) = \Phi_{\text{in}} = \frac{\rho^2 - R^2}{4}\,, \tag{2.1}$$

and $\Phi = 0$ outside, where $\boldsymbol{\rho} = (\xi, x, y)$ and $\xi = z - v_0 t$. The transverse components of the vector potential A_x and A_y vanish due to the assumption of spherical symmetry. To avoid the discontinuity of electric field at the boundary, we introduce a smooth transition layer of width d at the edge of the bubble, $\Phi = \Phi_{\text{in}} + f(\rho, R, d)$, where $f(\rho, R, d)$ is chosen so that [29]

$$\frac{\partial \Phi}{\partial \rho} = -\frac{\rho}{4}\left(\tanh\frac{\rho - R}{d} - 1\right)\,. \tag{2.2}$$

For a non-evolving bubble, the electromagnetic potential Φ of the bubble depends on time only through the co-moving variable ξ. In contrast, the

potential of a slowly-evolving bubble has a weak explicit dependence on t. It is therefore convenient to introduce the normalized electrons moving-frame Hamiltonian [42, 43] given by

$$H(\mathbf{P},\boldsymbol{\rho},t)=\sqrt{1+(\mathbf{P}+\mathbf{A}(\boldsymbol{\rho},t))^2}-v_0P_z-\phi(\boldsymbol{\rho},t)\,, \tag{2.3}$$

where $\mathbf{P}$ is the electron canonical momentum, and the explicit dependence of H on t is assumed to be very weak, i.e., $|\partial H/\partial t|R/c\ll 1$. For a static bubble the Hamiltonian of every plasma electron remains constant as it is overtaken by the bubble, i.e., $H=1$ for initially quiescent plasma electrons.

The Hamiltonian equations of motion in the co-moving frame are given by

$$\frac{d\mathbf{P}}{dt}=-\frac{\partial H}{\partial\boldsymbol{\rho}}\,,\quad \frac{d\boldsymbol{\rho}}{dt}=\frac{\partial H}{\partial\mathbf{P}}\,. \tag{2.4}$$

Noting that $\Phi/2=A_z=-\phi$, the equations of motion in the transverse (ξ,y) plane are

$$\frac{d\xi}{dt}=v_z-v_0\,, \tag{2.5}$$

$$\frac{dy}{dt}=v_y\,, \tag{2.6}$$

$$\frac{dP_\xi}{dt}=-\frac{v_z+1}{2}\frac{\partial\Phi}{\partial\xi}\,, \tag{2.7}$$

$$\frac{dP_y}{dt}=-\frac{v_z+1}{2}\frac{\partial\Phi}{\partial y}\,. \tag{2.8}$$

By solving Eqs. (2.6-2.8), we have verified that no electron injection into the static bubble takes place unless the stringent condition on the bubble's radius $R/\sqrt{2}>\gamma_0$ [40] is met. As was shown earlier [41], the situation changes dramatically when the bubble expands as it propagates through the plasma.

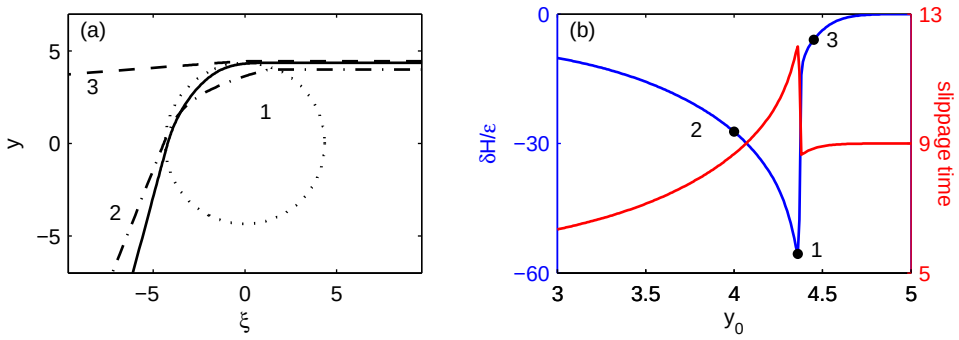

Figure 2.1: (a) In-plane ($x = 0$) orbits of initially quiescent electrons in the field of a non-evolving bubble with a radius $R = 4.2$ and Lorentz factor $\gamma_0 = 100$. The dotted circle is the bubble boundary. The trajectory of the most deflected electron (impact parameter $y_0 = 4.36$) is a thick solid line. Self-injection is not observed. (b) Expected change in Hamiltonian (blue) and slippage time (red) as a function of impact parameter (markers corresponding to the trajectories from panel (a) and are numbered accordingly).

In order to understand electron injection into an evolving bubble, we assume the simplest possible model of the bubble's evolution in which the only time-varying parameter of the bubble is its radius, which varies according to $R = R(t)$. Hence, the Hamiltonian of an electron given by Eq. (2.3) depends explicitly on time through the dependence of the potential Φ on $R(t)$. Then, Eqs. (2.6-2.8) must be numerically integrated in order to quantify the self-injection and trapping conditions for initially quiescent electrons. Throughout the rest of the chapter, plasma electrons ahead of the incident plasma bubble are assumed to be quiescent, with $H_{\rm in} = H(\xi = +\infty) = 1$.

2.2.2 Electron trapping by an expanding bubble

In this Section the bubble is assumed to grow linearly in time according to $R(t) = R_{\rm in}(1 + \epsilon t)$, where $R_{\rm in}$ is the initial radius, and $\epsilon \ll 1$ is the growth rate. At some instant in time $t_{\rm stop}$ the expansion is assumed to stop, and the radius is kept constant at the final value of $R_{\rm fin} = R(t_{\rm stop})$. The calculations are done in the Galilean frame co-moving with the bubble. In this frame, electrons are launched far away from the bubble ($\xi_{\rm ini} \gg 1$) in the (ξ, y) plane with the relative velocity $\mathbf{v} = -v_0\mathbf{e}_z$ and different impact parameters y_0. The typical simulation geometry is shown in Fig. 2.1(a). Because the potential is changing in time, the Hamiltonian is not conserved during the course of the interaction, evolving according to $dH/dt = \partial H/\partial t$. As the potentials vanish at a large distance, the Hamiltonian of a non-trapped particle must be positive far away from the bubble since $H(\rho \to \infty) = \sqrt{1 + \mathbf{P}^2} - v_0 P_z > 0$. Thus, all electrons with negative $H_{\rm fin} = H(t_{\rm stop})$ must remain confined inside the bubble at all future times, and $H_{\rm fin} < 0$ is a sufficient trapping condition. If the bubble expands rapidly enough, the Hamiltonian of some electrons changes by

$$\Delta H \equiv \int dt \frac{\partial H}{\partial t} = \int \frac{d\xi}{v_0 - v_x} \frac{\partial H}{\partial t} = \epsilon R_{\rm in} \int \frac{d\xi}{v_0 - v_x} \frac{\partial H}{\partial R} < -1\,, \qquad (2.9)$$

and these particles become trapped in the bubble. It can be shown that the integral in the right-hand-side of Eq. (2.9) is always negative, so that the bubble must expand ($\epsilon > 0$) for trapping to occur. Eventually, the trapped particles reach the center of the bubble and gain the peak energy $\gamma_{\rm max}$ calculated [29] as

$$\gamma_{\rm max} \sim \gamma_0^2 R^2/2\,. \qquad (2.10)$$

The time that the trapped electron takes to reach the center of the bubble is referred to as the dephasing time.

Initial parameters of the bubble provide enough information to estimate the minimal expansion rate sufficient for particle trapping, and to find the range of impact parameters from which the electrons can become trapped. This is achieved by relating the change in Hamiltonian sufficient for trapping ($|\delta H_\epsilon| \sim 1$) to the expected expansion rate ϵ. Using Eq. (2.9), we carry out integration along the electron trajectories in the field of a non-evolving bubble with $R = R_{\rm in}$, and arrive at the threshold expansion rate

$$\epsilon_{\rm tr} = \min_{y_0} |\delta H_\epsilon/\epsilon|^{-1} \,, \tag{2.11}$$

where

$$\delta H_\epsilon/\epsilon = R_{\rm in} \int \frac{\partial H}{\partial R} \frac{d\xi}{v_0 - v_x} \,. \tag{2.12}$$

For $\epsilon \ll 1$ it is expected that $\delta H_\epsilon \approx \Delta H \propto \epsilon$, which makes $\delta H_\epsilon/\epsilon$ independent of ϵ.

Another indicator of possible trapping is the interaction time between the electrons and the non-evolving bubble (slippage time),

$$T_{\rm slip} \equiv \int \frac{d\xi}{v_0 - v_x} \,. \tag{2.13}$$

Electrons with the largest slippage time are likely to get trapped in the expanding bubble. The predictive capability of these tools is examined in Figs. (2.1,2.2). It is interesting to note that trapping of initially quiescent electrons by a relativistically moving bubble is quite different from the classic problem of trapping

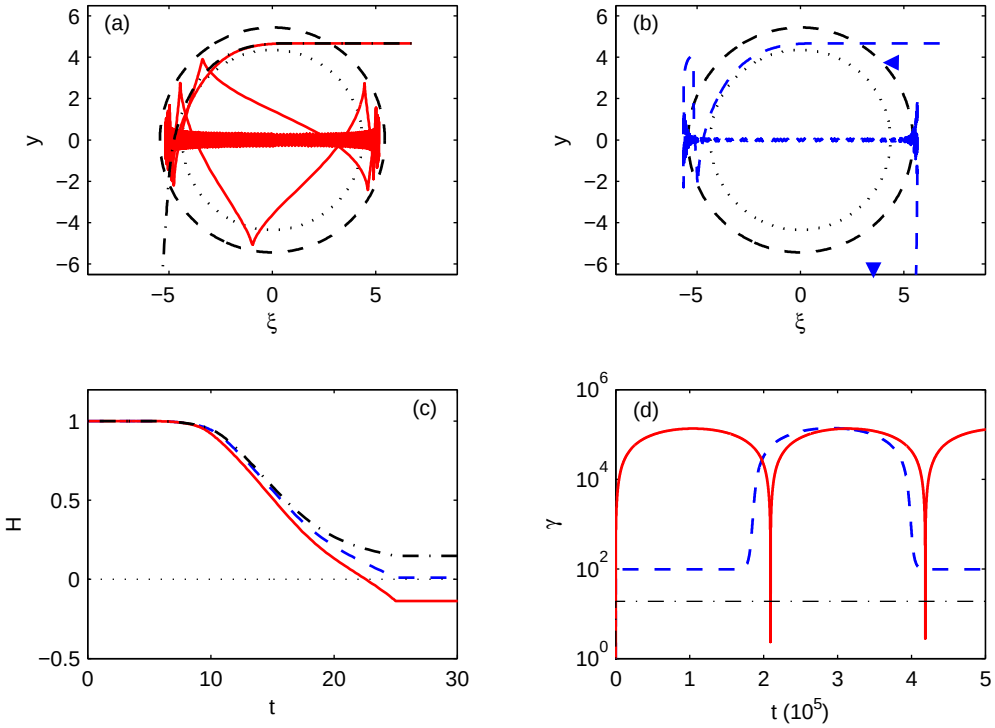

Figure 2.2: Self-injection and acceleration of electrons in the expanding bubble with the initial parameters from Fig. 2.1, and $\epsilon = 0.01$. Initial and final bubble radii are indicated with dotted and dashed circles in panels (a) and (b). (a) Orbits of trapped (red, solid) and passing (black, dash-dotted) electrons. (b) Orbit of an injected non-trapped electron (blue, dashed). (c) Temporal variation of the Hamiltonian. Trapped electron (red, solid) has $H_{\rm fin} = -0.14$, injected/non-trapped (blue, dashed) has $H_{\rm fin} = 0.01$, and passing (black, dash-dotted) $H_{\rm fin} = 0.15$. (d) Temporal variation of electron energy. Trapped electron energy oscillates with the dephasing period, while the non-trapped particle reaches the peak only once, and soon after that exits the bubble with $\gamma \approx 120$.

by an immobile potential well [44]. In the latter case, trapping occurs even when the potential changes adiabatically slowly while in the former case the bubble must expand faster than a threshold rate.

To emphasize the importance of bubble expansion for trapping, we consider an ultra-relativistic bubble ($\gamma_0 = 100$) of a moderate initial size, $R_{\rm in} = 4.2 \ll \gamma_0$ with a transition layer of thickness $d = 0.15$. Fig. 2.1(a) displays several electron trajectories with different impact parameters interacting with a non-evolving bubble. Self-injection is not observed for any value of the impact parameter y_0. The most deflected electron trajectory plotted with a thick solid line in Fig. 2.1(a) experiences an energy gain of $\gamma_{\rm fin} = 26 \ll \gamma_{\rm max}$. The quantity $|\delta H_\epsilon/\epsilon|$ evaluated for various impact parameters are plotted in Fig. 2.1(b). The expansion rate sufficient for trapping given by Eq. (2.11) is $\epsilon_{\rm tr} \approx 0.018$. Electrons are likely to be trapped from a narrow range of impact parameters around $y_0 = 4.36$, which corresponds to the trajectory of the most deflected electron in the non-expanding bubble. The slippage time $T_{\rm slip}$ is also shown in Fig. 2.1(b), indicating that the electrons with large $|\delta H|$ are the ones that interact with the bubble the longest.

The physical meaning of the trapping condition thus becomes clear: the bubble must be expanding rapidly enough to change its size by an appreciable fraction during the slippage time of an electron through the bubble. In the example shown in Fig. 2.1, the bubble should expand by $\epsilon_{\rm tr} T_{\rm slip} \approx 18\%$. For a minority of initially quiescent plasma electrons, $|\delta H_\epsilon/\epsilon| \gg 1$, and this small number of electrons are candidates for trapping in a slowly expanding bubble.

For the majority of electrons, $|\delta H_\epsilon/\epsilon| \sim 1$. Therefore, massive electron trapping by a slowly expanding ($\epsilon \ll 1$) bubble is not expected and most electrons are merely part of a quasi-static flow which supports the bubble fields.

Fig. 2.2 shows electron self-injection and acceleration in the field of an expanding bubble. Initial parameters for the bubble are the same as in Fig. 2.1. The bubble expands by 25% to $R_{\rm fin} = 1.25R_{\rm in}$, after which the expansion stops. The expansion rate is $\epsilon = 0.01$, which is somewhat lower than the predicted $\epsilon_{\rm tr}$. Even this modest bubble expansion rate results in electron self-injection from a very narrow range of impact parameters $y_0 \approx 4.6683 \pm 0.0035$.

2.2.3 Trapped, injected and passing electrons

Further analysis of particle trajectories shows that the electrons interacting with the bubble can be divided into three distinct groups. The largest one consists of the *passing* electrons with positive final Hamiltonians. One representative passing orbit is pictured in Fig. 2.2(a) with a black dash-dotted line. The corresponding time evolution of the Hamiltonian is shown in Fig. 2.2(c), with $H_{\rm fin} = 0.15$. This passing electron gains an energy $\gamma_{\rm fin} = 19 < \gamma_0$ during its slippage time, and is then deflected out of the bubble. Another group consists of the *trapped* electrons with negative final Hamiltonians. The trajectory corresponding to the lowest final Hamiltonian, $H_{\rm fin} = -0.14$, is plotted in Fig. 2.2(a) with a red solid line. This electron remains inside the bucket at all times, and its energy oscillates as indicated in Fig. 2.2(d). The third group consists of the electrons *injected* into the bubble, but not trapped for an

indefinite time. For the injected particles, $H_{\rm fin} > 0$. Injected electrons can stay in the bubble long enough to get accelerated to the same peak energy as the trapped particles. One such orbit (with $H_{\rm fin} = 0.01$) is shown in Fig. 2.2(b) with a blue dashed curve. The electron accelerates to a high peak energy, crosses the bubble center, decelerates, and eventually exits near the front end with $\gamma_{\rm fin} = 120$, which is slightly above γ_0 (see Fig. 2.2(d)).

For the remainder of this chapter, we will refer to these three groups as *passing* ($H_{\rm fin} > 0$, accelerated only up to $\gamma_{\rm fin} < \gamma_0$), *trapped* ($H_{\rm fin} < 0$, accelerated up to $\gamma_{\rm max}$), and *injected* ($H_{\rm fin} > 0$, not strictly trapped, also accelerated up to $\gamma_{\rm max}$)) electrons. *Self-injected* refers to either trapped or injected electrons, i.e., electrons which enter the bubble and eventually cross the center of the bubble, so that they are accelerated to the maximum possible energy $\gamma_{\rm max} \sim \gamma_0^2 R^2/2$.

Of these three groups, passing electrons gain the least energy as a result of interaction with the bubble. In the example orbit shown in Fig. 2.2(a) (black dash-dot line), the final energy is $\sim$ 19 MeV. The peak energy $\gamma_{\rm max}$ attained by the other two groups, trapped and injected electrons, is much higher than that for passing electrons, as shown in Fig. 2.2(d). The peak energy is achieved when the electron crosses the bubble center plane $\xi = 0$. The time $t_{\rm deph}$ required for the electron to cross the distance from the bubble edge ($\xi \approx -5$) to the bubble center is the dephasing time. In practice, the plasma length is chosen close to or below the dephasing length to ensure the optimal energy gain. In the case shown in Fig. 2.2, $L \approx ct_{\rm deph} \approx 170$ cm, and

the peak energy for both trapped and injected electrons is ~ 70 GeV.

It is important to note that for weakly-relativistic bubbles the injected electrons with positive H may stay in the bubble and gain the same energy as the trapped electrons. Such electrons exist even for a non-evolving bubble when energy conservation prohibits trapping from the quiescent background, and $H = 1$ for all the electrons. Self-injection in this case requires relatively large bubbles with $\gamma_0 \lesssim R/\sqrt{2}$ [40]. Conversely, in the opposite limit of $\gamma_0 \gg R$, any injected electron must be on the verge of trapping ($\Delta H \approx -1$). For instance, in the example shown in Fig. 2.2, all electrons with $\Delta H > -0.99$ are passing. Thus, in the ultrarelativistic limit of large γ_0, $\Delta H \leq -1$ is a necessary and sufficient condition for high energy acceleration with a high degree of accuracy, within the constraints of the idealized model of a spherical bubble.

Below we explore the transition between these two limiting cases of the moderately-relativistic and highly-relativistic plasma bubbles, establishing numerically the threshold condition for self-injection when strict trapping (i.e., $H < 0$) is not necessary for acceleration. Keeping the normalized initial radius the same, $R_{\rm in} = 4.2$, and expanding the bubble by 25% ($R_{\rm fin} = 1.25 R_{\rm in}$), we scan the Lorentz factor γ_0. For each value of γ_0, we find the *minimal* expansion rate $\epsilon_{\rm min}$ such that at least one electron becomes trapped. For this trajectory we perturb the impact parameter y_0 until we find the electron with the least change in Hamiltonian $|\Delta H|$ such that it stays in the bubble after the dephasing time, i.e., $\rho(t_{\rm deph}) < R_{\rm fin}$ (note that this electron is injected, but not

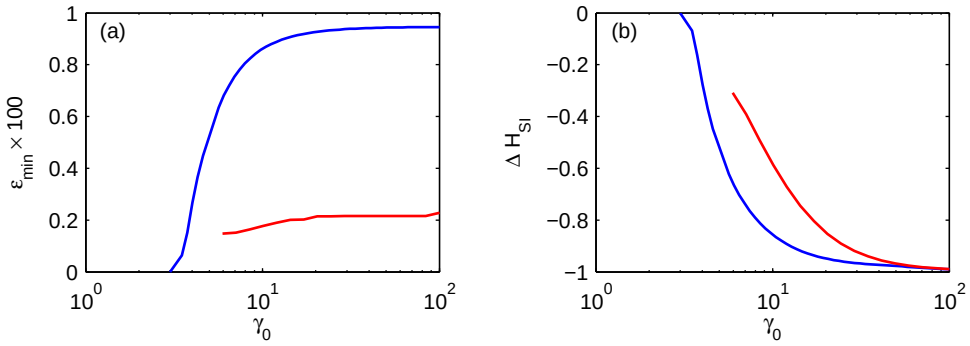

Figure 2.3: (a) Minimal expansion rate sufficient for *trapping* and (b) minimal change in Hamiltonian sufficient for *injection* in a bubble with Lorentz factor γ_0. Blue curves correspond to a spherically symmetric bubble, while red curves correspond to a spherical bubble with an localized "spike" in potential in the tail region of the bubble. Initial and final radii of the bubble are $R_{\rm in} = 4.2$ and $R_{\rm fin} = 1.25R_{\rm in}$, as in Fig. 2.2. For $\gamma_0 < R_{\rm in}/\sqrt{2}$ electrons are self-injected even into a non-evolving bubble. For $\gamma_0 \sim 100$, the self-injection threshold tends to the trapping threshold ($\Delta H \to -1$).

trapped). The change in Hamiltonian of this electron $\Delta H_{\rm SI}$ is the threshold for self-injection. Threshold curves $\epsilon_{\rm min}(\gamma_0)$ and $\Delta H_{\rm SI}(\gamma_0)$ are displayed in Fig. 2.3 (blue lines).

We see that at $\gamma_0 \lesssim R/\sqrt{2}$ self-injection does not require bubble evolution ($\epsilon_{\rm min} = 0$) so that $\Delta H_{\rm SI} = 0$, in agreement with the predictions of Refs. [29, 40]. For larger γ_0 bubble expansion becomes necessary, which leads to Hamiltonian reduction. In this intermediate range of moderately relativistic bubbles ($\gamma_0 \gtrsim R_{\rm in}/\sqrt{2}$) injected (but not trapped) electrons may constitute a considerable fraction of the accelerated electron beam. Finally, in the limit of very large γ_0, the bubble must grow the most rapidly ($\epsilon_{\rm min} \to 0.0095$), and the required change in the Hamiltonian tends to the trapping threshold, $\Delta H_{\rm SI} \to -1$. In this limit self-injection requires trapping by an evolving bubble.

When more detailed structure of the bubble potential is taken into account the curves in Fig. 2.3 shift to the right. The red curves in Fig. 2.3 are the threshold curves taking into account the modification to the potential structure explored in Ref. [29]. In this case, the density spike in region near the tail of the bubble is taken into account by adding a potential "bump" of the form $\Phi_p = \Phi_0 \exp\left[-((\xi - \xi_0)^2 + x^2 + y^2)/r_p^2\right]$. Here, we have taken $\Phi_0 = 1.0$, $\xi_0 = -(R + d)$ and $r_p = d$; this choice in ξ_0 reflects the fact that the spike in potential is near the tail of the bubble. The effect of this shift is that more electrons are injected but not trapped, and that trapping occurs for bubbles expanding at a slower rate. While this suggests that taking the

detailed bubble structure into account is important for accurate calculation of threshold expansion rates, the above method is purely phenomenological and the spherical potential with the Gaussian spike in the tail is formally not a solution of Maxwell's equations. A more realistic model of the bubble that self-consistently takes into account the fine bubble structure will be considered in Chapter 3.

As previously mentioned, the Lorentz factor of the bubble can be associated with the group velocity of the laser drive pulse, and hence with the plasma density, through $\gamma_0 = \sqrt{n_c/n_0}$, where $n_c = \omega_0^2 m_e/(4\pi e^2)$ is the critical density. The limit of large γ_0, where the self-injection threshold tends to the trapping threshold $\Delta H = -1$, corresponds to very rarefied plasmas; $\gamma_0 > 100$ implies $n_0 < 10^{17}$ cm^{-3} for the laser wavelength 1.05 μm. Such low densities are favorable for LWFA due to the relatively long dephasing length; self-guided bubble regime acceleration at these densities requires the use of petawatt lasers due to the high power requirement for relativistic self-focusing in rarefied plasmas.

2.2.4 Phase space rotation and generation of monoenergetic electron beams

We have established that for $\gamma_0 > R/\sqrt{2}$, electron self-injection is possible only for an expanding bubble. It follows that, stabilization of the bubble size clamps the self-injection process. Therefore, a bubble that undergoes a brief period of growth followed by a period of stability contains a short con-

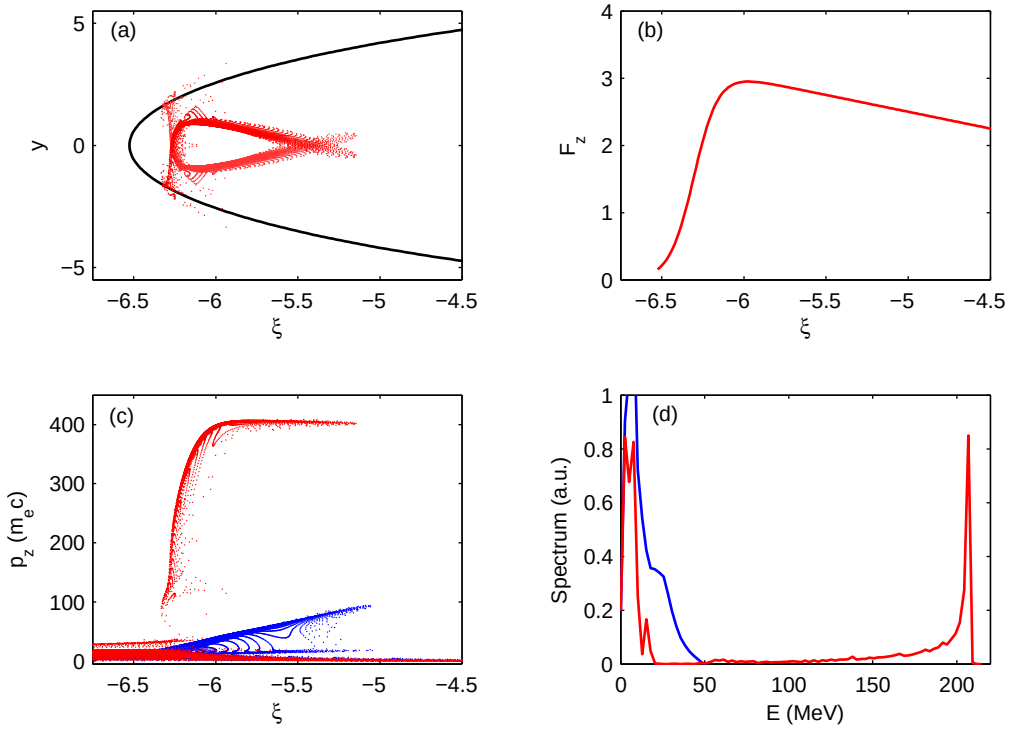

Figure 2.4: Generation of a monoenergetic beam due to the phase space rotation caused by the stabilization of bubble evolution. Parameters are the same as in Fig. 2.2, except that the bubble grows by 50% over the interval $0 < t < 50$, and then stabilizes. (a) Boundary of the bubble (black line) and position of trapped electrons (red dots) at $t = 175$. (b) Accelerating gradient of bubble on axis after stabilization ($t > 50$). The accelerating force on electrons is the largest near the edge of the bubble, and drops linearly towards the center. (c) Longitudinal phase space of trapped electrons and (d) corresponding energy spectrum at $t = 55$ (blue) and $t = 175$ (red).

tinuous self-injected electron bunch, which approximately spans the interval $-R_{\rm fin} < \xi < -R_{\rm in}$. Such a bunch is shown with red markers in Fig. 2.4(a) for the parameters of Fig. 2.2, except that the bubble was allowed to grow by 50% (only electrons with energy above 50 MeV are shown). During and immediately after the period of expansion, the self-injected electrons are characterized by a 100% momentum and energy spread (shown in blue Figs. 2.4(c,d) at $t = 55$). Electrons at the head of the bunch are self-injected earlier and thus have a higher momentum than those that are self-injected later. However, since the accelerating force on axis scales linearly with ξ inside the bubble, $F_z \equiv -\partial\Phi/\partial\xi \sim -\xi/2$ (see Fig. 2.4(b)), electrons self-injected later into a larger-sized bubble are accelerated the most strongly. As soon as the bubble stops growing, this non-uniform accelerating gradient starts rotating the electron phase space; the bunch tail gains energy relative to the bunch head. The result is the formation of a monoenergetic electron beam, as shown in red in Figs. 2.4(c,d) at time $t = 175$.

Non-stationary Hamiltonian analysis sheds further light on the phase space rotation of accelerated electrons as they advance deeper into the expanding bubble. The Hamiltonian (2.3) of a self-injected electron can be written $H \approx \gamma(1 - v_0) + \Phi$, where $v_0 \approx 1$ and $p_z \approx \gamma$. The energy of an electron on axis $(x, y = 0)$ inside the bubble at position ξ is

$$\gamma(\xi) \approx 2\gamma_0^2[H(\xi) - \Phi(\xi)], \tag{2.14}$$

where we have used the approximation $1 - v_0 \approx 1/2\gamma_0^2$. If the bubble is not evolving, then $H = 1$ for all electrons, so that for two self-injected electrons at

$\xi_1 < \xi_2 < 0$, it follows from (2.14) that $\gamma(\xi_1) < \gamma(\xi_2)$ since Φ is monotonically decreasing inside the bubble when $\xi < 0$. Thus, if beam loading [45, 46] can be neglected, the phase space of an accelerated electron bunch inside a non-evolving bubble cannot flatten before the dephasing time $t_{\rm deph}$. However, if the bubble expands during the time interval $0 < t < t_{\rm stop}$, then for $t > t_{\rm stop}$ the Hamiltonian of each electron is $H(t = t_{\rm stop})$. In this case, $H(\xi_1) > H(\xi_2)$ for two electrons at $\xi_1 < \xi_2 < 0$, since the earlier self-injected electron 2 experiences more bubble expansion than electron 1. It is therefore possible that $\gamma(\xi_1) = \gamma(\xi_2)$ for some time $t < t_{\rm deph}$, representing the generation of a monoenergetic electron bunch.

2.3 Self-consistent modeling of the trapping process

In this Section, the concepts introduced in Sec. 2.2 are examined quantitatively in a realistic numerical experiment. The key change in the model is a fully self-consistent description of laser-plasma interaction based on quasistatic PIC simulation and inclusion of the effects of the laser field on the test electrons. We simulate the laser and bubble evolution in a 3D cylindrical geometry using the PIC code WAKE [42]. The code describes the laser propagation in an extended paraxial approximation (group velocity dispersion of radiation in plasma is included), which is adequate for beams focused well above the diffraction limit. Plasma macroparticles are treated using the quasistatic approximation, and the laser acts on them through the time-averaged ponderomotive force. The quasistatic approximation implies conservation of

the Hamiltonian (2.3), hence macroparticles cannot be self-injected. We model self-injection using a non-quasistatic, relativistic, fully 3D test-particle tracking module incorporated in WAKE. With the test particle approach, the effects of beam loading [47] are neglected; however, this is a valid approximation in the limit of small beam charge. Initially quiescent test electrons are placed before the pulse and then interact with the laser ponderomotive force and the slowly varying bubble potentials. The effect of the laser field on the test electrons is described using the time-averaged ponderomotive potential. These approximations make the described numerical toolkit extremely fast and essentially noiseless.

Laser and plasma parameters of the following simulation roughly correspond to those of the Texas Petawatt laser [48] in the low-density plasma regime where the best quality GeV electron beams are expected. In this simulation, a 200 J, $\tau_L = 150$ fs laser pulse is focused to a spot size of $w_0 = 27$ μm in a plasma of density $n_e = 10^{17}$ cm^{-3}. The laser power is 1.3 PW, and the peak normalized vector potential $a_0 = |e|A/(m_e c^2) = 9.62$. The Lorentz factor associated with the laser group velocity is $\gamma_0 = 100$.

Fig. 2.5 demonstrates self-injection into a growing bubble. The laser defocuses over the first $\sim$ 3.2 mm of propagation, its intensity decreases as shown in Fig. 2.5(a) (black line), and the spot size increases (as is clear from comparison of Figs. 2.5(b,c)). This laser diffraction leads to bubble expansion. For this realistic bubble there is an absence of spherical symmetry, so the bubble length is defined as the distance from the first potential maximum to the

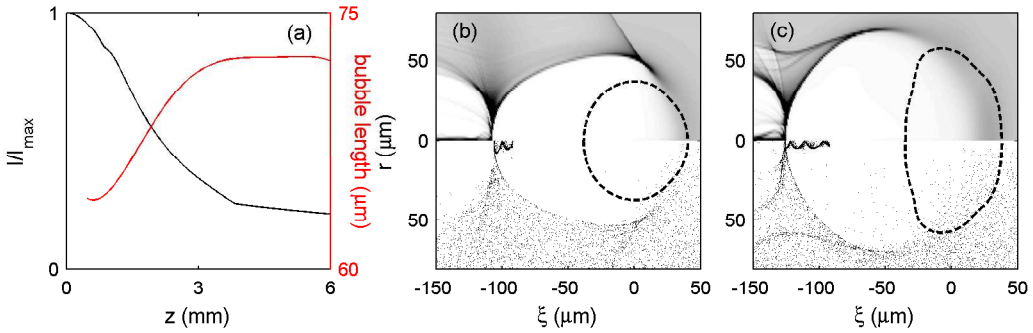

Figure 2.5: WAKE simulation of self-injection into a plasma bubble expanding due to a diffracting laser driver. (a) Normalized peak laser intensity (black) and bubble length (red) versus propagation distance z. Plasma density (top, linear grayscale) and position vectors of test electrons (bottom, dots) at (b) $z = 2$ mm and (c) $z = 5$ mm. Grayscale is cut off at $n_e = 5n_0 = 5 \times 10^{17}$ cm^{-3}. Dashed line: iso-contour of laser intensity at e^{-2} of the maximum.

first minimum on axis. This bubble length is shown as a function of propagation distance in Fig. 2.5(a) (red line). As the laser diffracts, the bubble length grows from $L_{\rm in} = 63.8$ μm to $L_{\rm fin} = 72.2$ μm. Test electrons are continuously self-injected during this period, and stops as soon as bubble expansion terminates as the laser becomes self-guided. This is shown in Fig. 2.6(b) by tracking the initial positions of test electrons. Self-injected electrons are shown in the middle of the self-injection process ($z = 2.0$ mm) in Fig. 2.5(b), and after the bubble stabilization ($z = 5.0$ mm) in Fig. 2.5(c).

An additional simulation was performed with the same initial conditions and plasma parameters, in which the laser pulse evolution was artificially turned off, so that the "frozen" laser and bubble traveled through the plasma at the laser group velocity. No evidence of self-injection into this static bubble

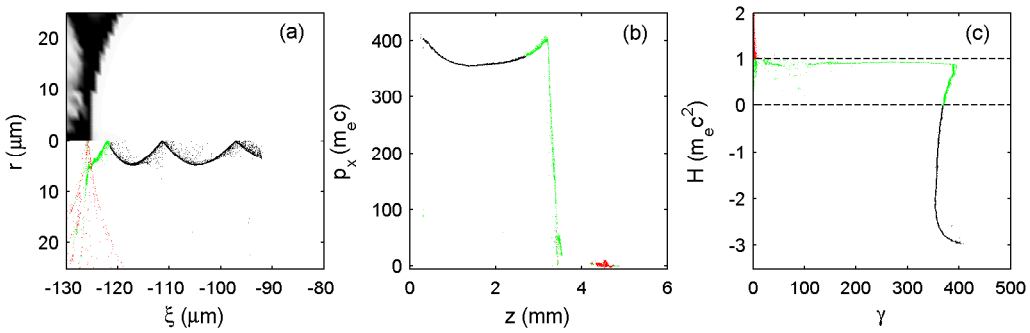

Figure 2.6: Hamiltonian diagnostics of electron self-injection and trapping from the simulation of Fig. 2.5 (all snapshots at $z = 5$ mm). Test electron markers are color-coded according to the value of their Hamiltonian: $H < 0$ (black), $0 < H < 1$ (green), and $H > 1$ (red). (a) Close-up of the base of the bubble from Fig. 2.5(c). Top: electron density in grayscale. Bottom: test electron position vectors. (b) Longitudinal momentum of test electrons at $z = 5$ mm vs. initial position in plasma. Termination of the bubble growth at $z \sim 3.2$ mm clamps the self-injection. (c) Hamiltonian versus energy of test electrons.

was observed, demonstrating the critical importance of bubble evolution in facilitating injection at low plasma densities.

2.3.1 Hamiltonian diagnostics of electron self-injection and trapping

We now verify the trapping condition from the Hamiltonian formalism in Eq. (2.9) using PIC simulation results from WAKE. Fig. 2.6(a) shows a close-up of the region around the tail of the bubble from Fig. 2.5(c) with the test electrons color coded according the value of their Hamiltonian. Black markers show particles with $H < 0$, green correspond to $0 < H < 1$, and red to $H > 1$. All the test electrons begin with the initial Hamiltonian $H_{\rm in} = 1$.

Applying the classification for electrons introduced in Sec. 2.2.3, about half of the electrons inside the bubble (in black) have negative Hamiltonian and are thus trapped. Fig. 2.6(b) shows that these are trapped during the early stage of laser propagation ($z < 2.6$ mm). The other half of electrons inside and near the bottom of the bubble are injected (in green, see Figs. 2.6(a,c)). Fig. 2.6(b) shows that they were injected immediately before the bubble stabilization. Red electrons with $H > 1$ are passing. Both the trapped and injected electrons inside the bubble are accelerated. This simulation shows that, in contrast to the idealized spherically symmetric bubble in Sec. 2.2, *reduction* of the Hamiltonian ($H < 1$) is a necessary condition for self-injection when a realistic bubble potential and the laser ponderomotive potential are taken into account. Moreover, $H < 0$ remains the strongest condition sufficient for electron acceleration.

In Fig. 2.6, the earlier self-injected electrons (black) have a significantly smaller Hamiltonian because they experience the full bubble expansion. Therefore, their final energy is reduced by the factor $-2H\gamma_0^2$. On the other hand, the later self-injected electrons (green) have a larger Hamiltonian. Therefore, they will have a higher energy at the same relative position inside the bubble. We explain this effect in further detail in the next subsection.

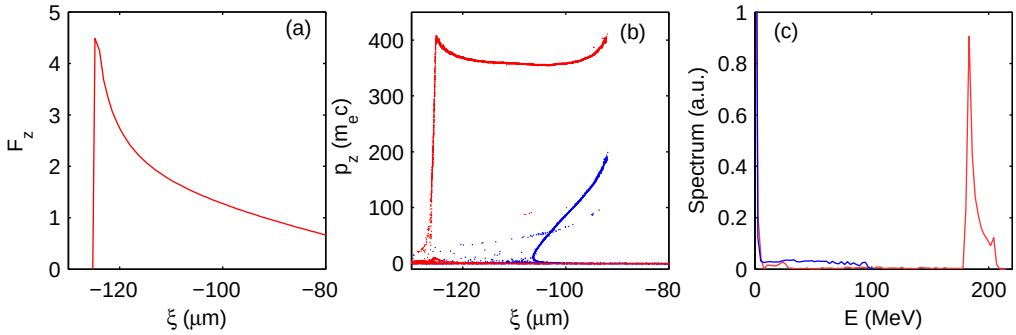

Figure 2.7: Demonstration of phase space rotation in the quasi-static PIC simulation with test electrons. (a) Accelerating gradient of bubble (in units $m_e\omega_p c/e^2$) on axis at $z = 5$ mm. (b) Longitudinal phase space of electrons at $z = 2$ mm (blue) and $x = 5$ mm (red), and (c) corresponding energy spectra.

2.3.2 Generation of a monoenergetic bunch due to phase space rotation

Phase space rotation reduces the large momentum spread generated during the self-injection process in the same way as described in Sec. 2.2.4. As the bubble expands, self-injection goes on without interruption. As a consequence, electron momentum and energy spectra are continuous (shown in blue in Figs. 2.7(b,c)), and electrons self-injected earlier have the highest momentum and energy. As the expansion stops and the self-injection terminates, the electron bunch is exposed to a longitudinally non-uniform accelerating gradient as shown in Fig. 2.7(a). Variation of the gradient along the bunch can be seen from comparison of Figs. 2.7(a,b) (red markers). Electrons in the tail of the bunch are exposed to a higher accelerating force, and approximately 2 mm after the bubble stabilization at $z = 5$ mm, the tail and the head of

the bunch gain the same energy as seen in Fig. 2.7(b) (red markers). Thus, a quasi-monoenergetic bunch is formed as seen in the red electron spectrum in Fig. 2.7(c). Further phase space rotation at larger propagation distances results in a degradation of the energy spectrum, because electrons at the tail of the bunch out-speed those at the head. Therefore, the length of the plasma must be properly optimized to give the narrowest energy spread.

2.4 Summary

This chapter has demonstrated that expansion of the bubble causes self-injection and acceleration of electrons from an ambient plasma. A sufficient condition for trapping in terms of Hamiltonian reduction and minimal expansion rate have been established within the framework of a simplified spherical bubble model. The dependence of this minimal expansion rate and Hamiltonian variation on the bubble Lorentz factor has been characterized. PIC simulations show that growth of the bubble due to the evolution of the laser driver is the dominant mechanism of self-injection for rarefied plasmas. Thus, bubble expansion is crucial for LWFA experiments with petawatt laser pulses, where rarefied plasmas with $k_p R \ll \gamma_0$ are required for laser self-guiding and self-injection is relied upon to create the monoenergetic electron bunch. Furthermore, stabilization of an expanding bubble generates a monoenergetic electron beam by terminating the self-injection process and bringing about phase space rotation due to the inhomogenous accelerating gradient experienced by the injected bunch.

Chapter 3

Self-injection beam driven wakefield accelerators

3.1 Plasma wakefield acceleration

Electron beam driven plasma wakefield accelerators (PWFA) have attracted interest in recent years for their ability to substantially boost the maximum electron energy of existing accelerator facilities [8]. Such schemes aim to efficiently transfer the energy of an electron drive bunch (which excites the plasma wave) to that of a witness bunch (which is accelerated by the plasma wave). For such an "afterburner", it is beneficial to operate in the highly nonlinear bubble regime [38, 25] in order to take advantage of extremely high accelerating gradients, constant longitudinal accelerating fields [46], and focusing transverse fields. The bubble regime also introduces the possibility of self-injection, whereby initially quiescent background plasma electrons become trapped inside the accelerating phase of the plasma bubble.

In LWFA self-injection is often desirable because no external injectors are required, and the bubble expansion may occur naturally due to the nonlinear evolution of the laser pulse or be forced through a background plasma density downramp. In PWFA energy boosting schemes, self-injection may be

a parasitic effect to be avoided, since injected electrons produce a "dark current" of much lower energy than the witness bunch electrons. Since density downramps may cause bubble expansion, this places a limit on the background density inhomogeneities that can be tolerated in order to prevent dark current formation. On the other hand, self-injection may be considered as an alternative to witness beams.

This chapter analyzes the phenomenon of self-injection into a PWFA, where bubble expansion is due to a slow density downramp. An analytic model of the bubble fields is presented in Sec. 3.2 that takes into account the driver beam parameters, background density inhomogeneities, and the crucial role of the plasma return current. This analytic model, which gives globally applicable expressions for the wakefields in the bubble exterior and interior, is a crucial extension of previous work [39, 49] for bubble fields inside the bubble. Knowledge of the fields outside of the bubble enables us to calculate the trajectory of initially quiescent plasma electrons that become self-injected due to their interaction with the deepening potential well of the growing bubble. Sec. 3.3 contains an analysis of the self-injection process within a Hamiltonian framework [41, 50]. Results are found to be in good agreement to with particle-in-cell (PIC) simulations, and estimates of the threshold bubble expansion rates sufficient for trapping are presented.

3.2 Analytic model of bubble structure

3.2.1 Quasi-static approximation

We begin by defining several key dimensionless variables in normalized units, where time is normalized to ω_p^{-1}, length to $k_p^{-1} \equiv c/\omega_p$, charge and mass to the electron charge e and mass m, respectively, density to n_0, and potential to mc^2/e. Here $\omega_p^2 \equiv 4\pi e^2 n_0/m$, where n_0 is the background plasma density. Maxwell's equations for potentials in the Lorenz gauge are

$$\left(\frac{\partial^2}{\partial t^2} - \nabla^2\right) \left[\begin{array}{c} \mathbf{A} \\ \phi \end{array} \right] = \left[\begin{array}{c} \mathbf{J} \\ \rho \end{array} \right] , \tag{3.1}$$

where we have normalized the current and charge densities to ecn_0 and en_0 respectively. Transforming to the co-moving variables $(t, \xi \equiv t - z)$ and using the quasi-static approximation [51] $\partial_t \ll \partial_\xi$, we obtain the following simplification of Maxwell's equations [52, 53]:

$$-\nabla_\perp^2 \left[\begin{array}{c} \mathbf{A} \\ \phi \end{array} \right] = \left[\begin{array}{c} \mathbf{J} \\ \rho \end{array} \right] . \tag{3.2}$$

where the Lorenz gauge condition is given by

$$\nabla_\perp \cdot \mathbf{A}_\perp = -\frac{\partial \psi}{\partial \xi} , \tag{3.3}$$

and where $\psi \equiv \phi - A_z$. Cylindrical symmetry implies that $\mathbf{A}_\perp = A_r \hat{r}$, and the above gauge condition allows us to compute A_r from the pseudopotential ψ. Thus, for known source terms ρ and J_z, ψ and A_z can be calculated by solving the following equation:

$$-\frac{1}{r}\frac{\partial}{\partial r}\left(r\frac{\partial}{\partial r}\right) \left[\begin{array}{c} \psi \\ A_z \end{array} \right] = \left[\begin{array}{c} \rho - J_z \\ J_z \end{array} \right] , \tag{3.4}$$

and all non-vanishing fields can be obtained according to the following expressions:

$$E_z = \frac{\partial \psi}{\partial \xi}\,, \tag{3.5}$$

$$E_r = -\frac{\partial \phi}{\partial r} - \frac{\partial A_r}{\partial \xi}\,, \tag{3.6}$$

$$B_\theta = -\frac{\partial A_r}{\partial \xi} - \frac{\partial A_z}{\partial r}\,. \tag{3.7}$$

Below we introduce a simple model for the source terms in Eq. (3.4) both inside and outside the bubble. They are comprised of the charge densities of the beam, surrounding plasma and stationary ions, respectively given by ρ_{beam}, ρ_{elec} and ρ_{ion}, as well as the beam and current densities, $J_{z,beam}$ and $J_{z,elec}$, respectively.

3.2.2 Source terms

We define the density profile for the ultrarelativistic (and hence highly rigid) electron beam driver as

$$\rho_{beam}(\xi, r) \equiv J_{z,beam}/c = \frac{N}{(2\pi)^{3/2}\sigma_r^2\sigma_z} \exp\left(\frac{-r^2}{2\sigma_r^2} + \frac{-\xi^2}{2\sigma_z^2}\right), \tag{3.8}$$

where N is the number of beam electrons and $\sigma_{r,z}$ are the transverse and longitudinal widths of the beam, respectively. We take ions to be immobile, i.e., $\rho_{ion} = en_0$. Then, the total charge density is $\rho = \rho_{beam} + \rho_{elec} + \rho_{ion}$ and the total longitudinal current is $J_z = J_{z,beam} + J_{z,elec}$.

Next, we make assumptions about the current and density distribution of plasma electrons which will fully specify the source terms in Eq. (3.4). We

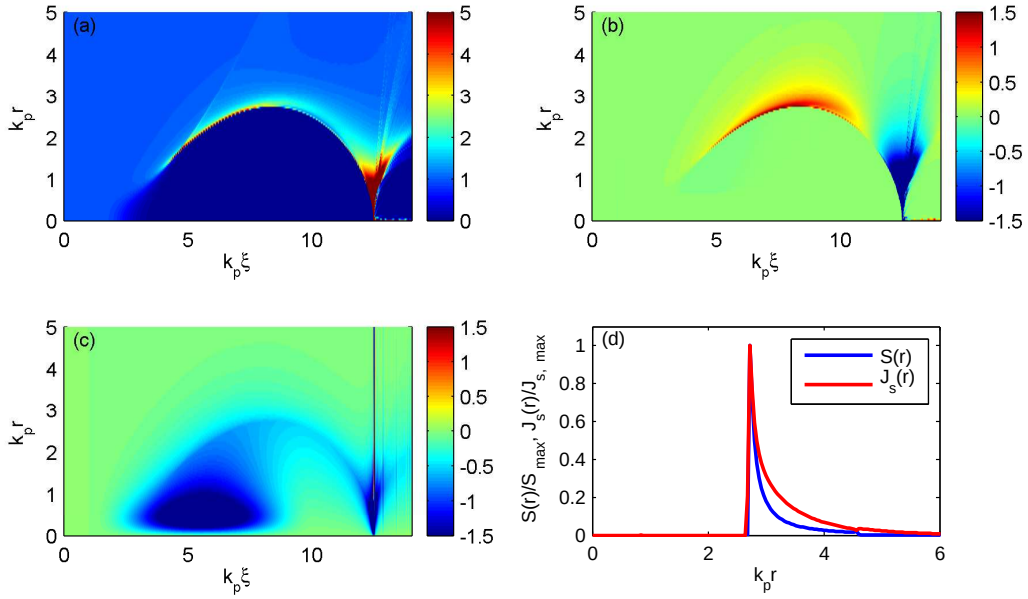

Figure 3.1: (a,b): Plasma electron and return current density from PIC simulation. The color scales in each subfigure are capped at different levels due to the large difference in the peak magnitude of the two quantities, i.e. $max(\rho_{elec}) \gg max(J_{z,elec})$. For simplicity, the contributions from the electron beam driver are not shown. (c): Azimuthal magnetic field B_θ. Unshielded B_θ extends to approximately k_p^{-1} outside the edge of the bubble. (d): Sheath density profile $S(\xi, r) \equiv -(\rho - J_z)$ and return current $J_s(r)$ for a transverse slice (fixed value of ξ) of the bubble (from PIC simulation). Here, S and J_s have been normalized by their maximal values to allow for comparison of their widths, since $S \gg J_s$.

assume that the drive beam causes complete cavitation of plasma electrons inside the bubble so that the bubble contains only ions, i.e., $\rho_{elec} = 0$ inside the bubble. This bubble is assumed to have a clearly defined boundary given by the function $r_b(\xi)$. As was demonstrated earlier [39, 49] $r_b(\xi)$ can be approximated by the trajectory of a single electron. We assume an exponential dependence $\rho_{elec} \approx \rho_s \exp\left[-(r - r_b(\xi))/\Delta_\rho\right]$ for the dense electron sheath layer immediately outside the bubble, where ρ_s is the peak sheath density. Here, Δ_ρ can be thought of as the characteristic decay length of the high density sheath layer, and Δ_ρ does not depend on ξ. These assumptions are justified by the plasma density profile observed in the PIC simulation WAKE [42], as shown in Fig. 3.1(a). We define the source term for Eq. (3.4) $S(\xi, r) \equiv -(\rho - J_z)$ as

$$S(\xi, r) = \begin{cases} -1 & (r < r_b(\xi))\,, \\ S_0(\xi) e^{-(r - r_b(\xi))/\Delta_\rho} & (r \geq r_b(\xi))\,, \end{cases} \tag{3.9}$$

where $S_0(\xi)$ is the value of the source function $S(\xi, r)$ at $r = r_b(\xi)$. We note here that $\rho - J_z \approx \rho$ is consistently observed in PIC simulations, so that the length scale for the source term $S(\xi, r)$ is very close to that for the electron density ρ_{elec}. To complete our description of the source terms we must now take into account the plasma return current in the sheath layer, so that the total longitudinal current is

$$J_z(\xi, r) = J_{z,beam}(\xi, r) + J_s(\xi) e^{-(r - r_b)/\Delta_J} \theta(r - r_b)\,, \tag{3.10}$$

where Δ_J is the width of the sheath return current, $\theta(x)$ is the Heaviside function, and the function $J_s(\xi)$ represents the longitudinal structure of the

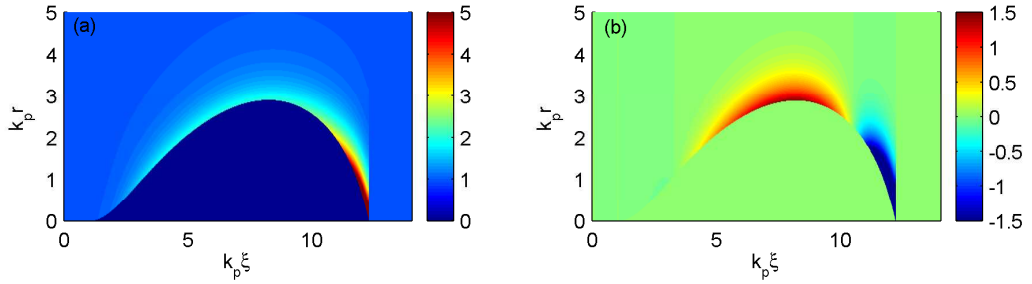

Figure 3.2: (a): Plasma electron density and (b): return current density $J_s(\xi)e^{-(r-r_b)/\Delta_J}\theta(r-r_b)$ from the analytic model, Eq. (3.15). For simplicity, the contributions from the electron beam driver are not shown.

return current. The existence of such a return current is consistent with PIC simulation results as shown in Fig. 3.1(b). The return current shields the the displacement current inside the bubble so that the azimuthal magnetic field B_θ vanishes at $r \to \infty$. Taking this return current into account is crucial for the extension the model to the exterior of the bubble, since the unshielded magnetic field within the return current layer $r_b(\xi) < r < r_b(\xi) + \Delta_J$ plays an important role in determining the trajectories of electrons that stream along the edge of the bubble and become candidates for self-injection. Extension of the magnetic field B_θ outside the bubble edge is also observed in PIC simulations, as shown in Fig. 3.1(c). We have assumed here that the return current decays exponentially for $r \geq r_b(\xi)$ like $S(\xi, r)$ but has a different thickness Δ_J, as illustrated in Fig. 3.1(d). The introduction of separate length scales for $\rho - J_z$ and J_z is again justified since $\rho - J_z \approx \rho$.

The charge continuity equation $\partial\rho/\partial t + \nabla \cdot J = 0$ under the quasi-static

approximation can be expressed as [51]

$$\frac{\partial}{\partial \xi}(\rho - J_z) + \frac{1}{r}\frac{\partial}{\partial r}(rJ_r) = 0\,, \tag{3.11}$$

and since the second term clearly vanishes upon integration over the transverse plane, it follows that

$$\frac{\partial}{\partial \xi}\int_0^\infty S(r) r dr = 0 \tag{3.12}$$

for all values of ξ. This allows us to obtain

$$S_0(\xi) = \frac{r_b^2(\xi)}{2\Delta_\rho(r_b(\xi) + \Delta_\rho)}\,. \tag{3.13}$$

For $r \to \infty$, $B_\theta = -(\partial A_z/\partial r + \partial A_r/\partial \xi) = 0$, so that

$$\int_0^\infty J_z r dr + \int_0^\infty \frac{d^2\psi}{d\xi^2} r dr = 0\,. \tag{3.14}$$

It follows that the sheath layer current is given by

$$J_s(\xi) = \frac{\lambda(\xi) - \int_0^\infty r dr d^2\psi/d\xi^2}{\Delta_J(r_b + \Delta_J)}\,. \tag{3.15}$$

A plot of the sheath layer return current from Eq. (3.15) is shown in Fig. 3.2(b), which compares well with that from PIC simulation shown in Fig. 3.1(b).

3.2.3 Bubble fields

From the above assumptions, the source terms of Eq. (3.4) have been specified everywhere. It follows from the argument in Sec. 3.2.1 that all wake-fields can now be found. Solving Eq. (3.4) using the Green's function for the Laplace operator in cylindrical geometry it follows that

$$\psi(\xi, r) = -\int_r^\infty dr' r' S(\xi, r') \ln\frac{r}{r'}\,. \tag{3.16}$$

Thus, for the pseudopotential ψ we have the expression

$$\psi(\xi, r) = \frac{r_b^2 - r^2}{4} + \frac{\Delta_\rho r_b^2}{2(r_b + \Delta_\rho)} \left[1 + e^{r_b/\Delta_\rho} E_1 \left(\frac{r_b}{\Delta_\rho} \right) \right] \tag{3.17}$$

for $r < r_b(\xi)$ and

$$\psi(\xi, r) = \frac{\Delta_\rho r_b^2}{2(r_b + \Delta_\rho)} e^{-(r-r_b)/\Delta_\rho} \left[1 + e^{r/\Delta_\rho} E_1 \left(\frac{r}{\Delta_\rho} \right) \right] \tag{3.18}$$

for $r \geq r_b(\xi)$, where $E_1(x) \equiv \int_x^\infty e^{-t} t^{-1} dt$ is the exponential integral function. The exponential integral has the asymptotic behavior $e^x E_1(x) \to x^{-1}$ as $x \to \infty$. We note that the different expression in Eq. (3.17) from that given in Refs. [39, 49] is due to our different choice of density profile in the sheath layer. Similarly, from Eq. (3.4), we have

$$A_z(\xi, r) = \lambda(\xi) \ln r \tag{3.19}$$

for $r < r_b(\xi)$ and

$$\begin{aligned} A_z(\xi, r) =& \lambda(\xi) \ln r - J_s(\xi) \Delta_J \Bigg\{ r_b \ln \left(\frac{r}{r_b} \right) + \Delta_J \Bigg[-1 + \ln \left(\frac{r}{r_b} \right) \\ &+ e^{-(r-r_b)/\Delta_J} + e^{r_b/\Delta_J} \left(E_1 \left(\frac{r}{\Delta_J} \right) - E_1 \left(\frac{r_b}{\Delta_J} \right) \right) \Bigg] \Bigg\} \end{aligned} \tag{3.20}$$

for $r \geq r_b(\xi)$, where $\lambda = \lambda(\xi) \equiv \int_0^\infty r \rho_{beam}(\xi, r) dr$ is the linear charge density of the electron driver beam. The above expressions for A_z are valid for $r \gg \sigma_r$, which is not a strong restriction since the drive beam is thin, i.e., $\sigma_r \ll 1$. From the gauge condition given by Eq. (3.3), the radial component A_r is calculated as

$$A_r(\xi, r) = r \frac{\partial r_b}{\partial \xi} \frac{r_b(r_b^2 + 2\Delta_\rho r_b + 2\Delta_\rho^2)}{4(r_b + \Delta_\rho)^2} \left(1 + e^{r_b/\Delta_\rho} E_1 \left(\frac{r_b}{\Delta_\rho} \right) \right) \tag{3.21}$$

for $r < r_b(\xi)$ and

$$A_r(\xi, r) = \frac{1}{r}\frac{\partial r_b}{\partial \xi}\frac{r_b(r_b^2 + 2\Delta_\rho r_b + 2\Delta_\rho^2)}{4(r_b + \Delta_\rho)^2}\times$$
$$\left[\left(r_b^2 + 3\Delta_\rho r_b + 3\Delta_\rho^2 - r^2 e^{r_b/\Delta_\rho} E_1\left(-\frac{r}{\Delta_\rho}\right)\right) - 3\Delta_\rho(\Delta_\rho + r)e^{-(r-r_b)/\Delta_\rho}\right] \tag{3.22}$$

for $r \geq r_b(\xi)$. From the potentials ψ, A_z and A_r, the bubble fields are given by Eqs. (3.5-3.7). Details on calculation of the function $r_b(\xi)$ are presented in the next subsection

3.2.4 Bubble shape

Since the potentials are expressed in terms of the function $r_b(\xi)$, to complete the description of the bubble fields we must find $r_b(\xi)$. As noted earlier, $r_b(\xi)$ is approximately equal to the the trajectory of a single electron that travels along the edge of the bubble. For initially quiescent plasma electrons we have in the quasi-static limit the constant of motion [42] $\gamma - p_z - \psi = 1$, where γ is the relativistic factor, and $\mathbf{p}$ is the kinetic momentum. It follows that

$$\frac{d\xi}{dt} = 1 - v_z = \frac{1+\psi}{\gamma}\,, \tag{3.23}$$

and it can be shown that [42]

$$\gamma = \frac{1 + p_r^2 + (1+\psi)^2}{2(1+\psi)}\,. \tag{3.24}$$

From Eq. (3.23) the transverse momentum is given by

$$p_r = \gamma\frac{dr_b}{dt} = (1+\psi)\frac{dr_b}{d\xi}\,, \tag{3.25}$$

and the equation of motion for the trajectory $r_b(\xi)$ is

$$\frac{dp_r}{d\xi} = -\frac{\gamma}{1+\psi}(E_r - v_z B_\theta)\,, \tag{3.26}$$

where from Eqs. (3.5-3.7) for the wakefields,

$$-(E_r - v_z B_\theta) = \frac{\partial \psi}{\partial r} + \frac{1+\psi}{\gamma}\left(\frac{\partial A_r}{\partial \xi} + \frac{\partial A_z}{\partial r}\right)\,. \tag{3.27}$$

From Eqs. (3.24-3.27), and using the expressions for ψ, A_z and A_r given in Sec. 3.2.3, the equation of motion can then be rewritten entirely in terms of $r_b(\xi)$ and its derivatives:

$$A(r_b)\frac{d^2 r_b}{d\xi^2} + B(r_b) r_b \left(\frac{dr_b}{d\xi}\right)^2 + C(r_b) r_b = \frac{\lambda(\xi)}{r_b}\,, \tag{3.28}$$

where

$$\begin{aligned}
A &= 1 + \frac{r_b^2 \Delta_\rho (1+\alpha)}{2(r_b+\Delta_\rho)} + \frac{r_b(1+\alpha)}{4(r_b+\Delta_\rho)^3}\left[r_b^3 + 3r_b^2\Delta_\rho + 4r_b\Delta_\rho^2 + 2\Delta_\rho^3\right]\,, \\
B &= \frac{r_b}{4} + \frac{r_b}{2(r_b+\Delta_\rho)^2}\left[r_b^2\alpha + 2r_b\Delta_\rho\alpha + \Delta_\rho^2(1+2\alpha)\right] \\
&\quad + \frac{r_b}{4(r_b+\Delta_\rho)^3\Delta_\rho}[r_b^4\alpha + 4r_b^3\Delta_\rho\alpha + 7r_b^2\Delta_\rho^2\alpha \\
&\qquad\qquad + 2r_b\Delta_\rho^3(-1+2\alpha) + 2\Delta_\rho^4\alpha]\,, \\
C &= \frac{1}{4}\left[1 + \frac{1}{(1+\psi|_{r_b})^2}\right]\,,
\end{aligned}$$

and $\alpha \equiv e^{r_b/\Delta_\rho} E_1(r_b/\Delta_\rho)$. We note that our expressions for the coefficients A, B and C are modified from those given in Refs. [39, 49] due to our different choice of density profile in the sheath layer. Once Eq. (3.28) is integrated numerically the bubble wakefields can be calculated using the expressions from Sec. 3.2.3, and the trajectories of plasma electrons that interact with the bubble can be studied.

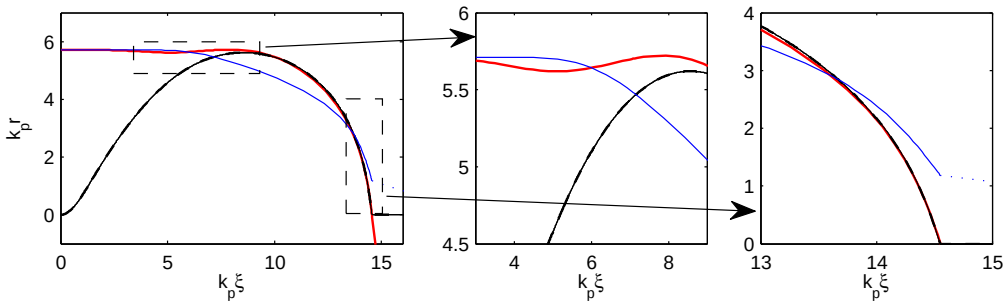

Figure 3.3: Electrons interacting with a non-evolving bubble (solid black) with parameters $\lambda_0 = 6$, $\sigma_z = \sqrt{2}k_p^{-1}$ and $\Delta_\rho = 0.5k_p^{-1}$, and with shielded (blue, $\Delta_J = 0.5k_p^{-1}$) and unshielded (red, $\Delta_J = k_p^{-1}$) magnetic field in the return current layer. The electron-bubble interaction length is longer in the unshielded case (red), where the electron follows along the edge of the bubble (see insets).

3.3 Electron trapping

3.3.1 Role of return current in determining particle trajectories

We now make use of the model wakefields to study the trapping of initially quiescent plasma electrons into an ultra-relativistic bubble. In order for the model to produce electron trajectories that closely match those from PIC simulations, it is critical that the return current thickness Δ_J is thicker than the density sheath thickness Δ_ρ. This is because the unshielded azimuthal magnetic field B_θ within the sheath current layer $r_b(\xi) < r < r_b(\xi) + \Delta_J$ affects the trajectories of electrons that stream close along the bubble boundary. Based on PIC simulations (see example in Fig. 3.1(d)) we have found that $\Delta_J \approx 2\Delta_\rho$ accurately reproduces the current and charge distributions surrounding the bubble. That $\Delta_\rho < \Delta_J$ is physically reasonable, since the

plasma forms a dense electron sheath to shield the positive charge of the bubble over approximately a Debye length $\lambda_D \equiv \sqrt{k_B T_e / e^2 n_0}$. On the other hand, the return current layer spreads out over a collisionless skin depth $k_p^{-1} > \lambda_D$, the characteristic length of the plasma wakefields.

Fig. 3.3 illustrates the role of the return current in determining the particle trajectories. Here, the bubble parameters are given by $\lambda_0 = 6$, $\sigma_z = \sqrt{2}$, and $\Delta_\rho = 0.5$. For the blue trajectory $\Delta_J = \Delta_\rho$, so that the sheath magnetic field is shielded and does not have an effect. In this case, the electron does not follow along the bubble edge but is pulled through the bubble by the electric fields of the ion column. As the particle passes behind the bubble, the model fields vanish, resulting in a discontinuity in the trajectory (blue dotted line). For the case of the red electron, $\Delta_J = 1 > \Delta_\rho$, and an unshielded B_θ in the sheath layer causes the electron to stream along the edge of the bubble. This unshielded magnetic field has the opposite effect of the electric field, pushing the electron away from the bubble. We have found that regardless of the electron initial radial offset r_0 (or impact parameter), the bubble-electron interaction length is always longer in the unshielded case (i.e., $\Delta_J > \Delta_\rho$). Since the electrons that are the most likely to become trapped are those that interact with the bubble the most strongly, the return current layer and its associated magnetic fields are important in determining the trajectories of trapped electrons. Trapping of initially quiescent plasma electrons by both frozen and growing bubbles will be analyzed in more detail in the following subsections.

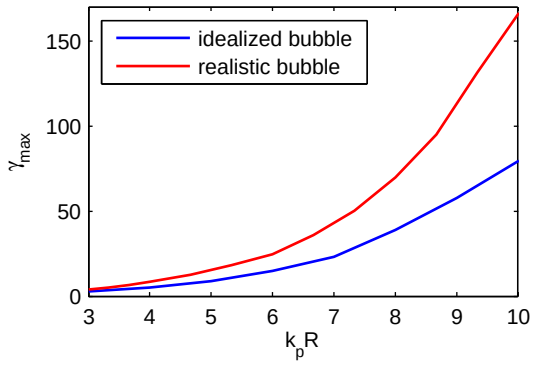

Figure 3.4: Maximum energy gain for a non-evolving bubble as a function of bubble size for a simplified spherical bubble model (blue) and the more realistic model described in this chapter (red). In both models the bubble has an ultrarelativistic velocity $v \to c$.

3.3.2 Trapping in a non-evolving bubble

Having demonstrated the importance of the azimuthal magnetic field surrounding the bubble for accurate calculation of particle trajectories, we now use our semi-analytic model to study electron trapping. Trapping studies within the context of analytic or semi-analytic models offer the advantage of lower numerical noise and more thorough parameter space scans when compared to PIC simulations. Previous works [29, 40] have shown using an idealized non-evolving spherical bubble model that self-injection is possible for large enough blowout radii, where the critical blowout radius scales linearly with the bubble relativistic factor γ_0. Other authors [54] have suggested (on the basis of PIC simulations) that when the radius exceeds several collisionless skip depths trapping always occurs even for non-evolving bubbles.

Using both the realistic model of the bubble described above as well as

an idealized spherical bubble model [29] we have performed parameter scans searching for injection in non-evolving bubbles for a wide range of bubble sizes. In the idealized model the bubble radius is simply an input parameter; in the realistic model the bubble size was determined by the drive beam parameter λ_0 while the beam length was limited to a small range near the resonance $\sigma_z \approx \sqrt{2}$. For the realistic model we further scanned the density sheath width in a small range near $\Delta_\rho \approx 0.5$ while keeping the return current width fixed at $\Delta_J = 1.0$. We note that in both models the bubble velocity was set equal to the speed of light.

The maximum electron energy gain for normalized bubble radii in the range $3 \sim 10$ is shown in Fig. 3.4. These passing electrons skirt the edge of the bubble and are accelerated for a propagation distance of a few bubble lengths, so they only experience moderate energy gain. Thus, in the ultra relativistic limit $v_0 \to c$ we do not see evidence of self-injection in static bubbles of normalized radii of order unity. However, this result does not contradict the conclusions of Refs. [29, 40] since for $\gamma_0 \to \infty$ no trapping is expected for finite bubble radii. Indeed, Fig. 3.4 suggests that injection can be expected for non-evolving bubbles of slower velocity such that $\gamma_0 < \gamma_{max}$. Bubbles with moderate values of γ_0 are of relevance in laser-driven wakefield accelerators, where the bubble velocity is determined by the laser group velocity, and may explain the injection observed in Ref. [54]. In this chapter, however, we are interested in bubbles driven by ultrarelativistic highly rigid electron beams with much larger relativistic factors. We shall therefore move on in the next

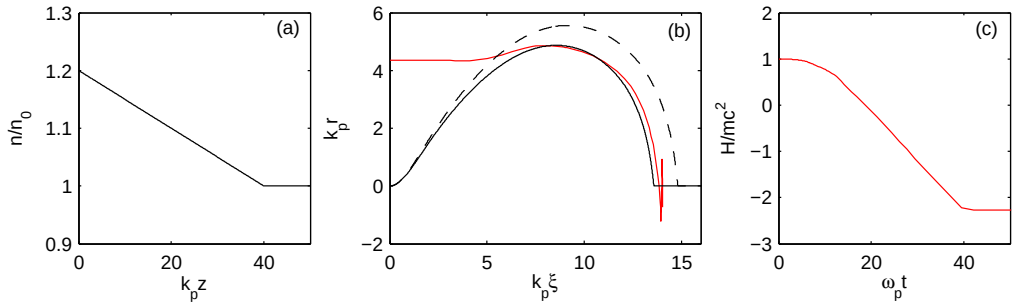

Figure 3.5: Electron trapping by a bubble growing due to a density downramp. (a): variation of the background plasma density along the propagation distance z. The downramp here is very gradual, i.e., $n^{-1}dn/dz \ll 1$. (b): initial (solid black) and final (dashed black) size of the bubble, and trajectory of trapped electron (red). Here, $\lambda_0 = 6$, $\sigma_z = 1.8k_p^{-1}$, $\Delta_\rho = 0.4k_p^{-1}$, $\Delta_J = k_p^{-1}$, $n_i = 1.2n_0$, $n_f = n_0$, and $L_{\rm ramp} = 40k_p^{-1}$. The impact parameter of the trapped electron is $r_0 = 4.36k_p^{-1}$. (c): electron moving-frame Hamiltonian. The electron becomes trapped once $H < 0$.

subsection to explore trapping for the case of evolving bubbles.

3.3.3 Trapping in an expanding bubble

We are interested in particular in self-injection of electrons that interact with the bubble while it is growing due to a background plasma density downramp. A density downramp enforces bubble evolution, since from force balance the maximum blowout radius can be estimated as

$$R(z) \approx r_{beam}\sqrt{\frac{n_{beam}}{n_{plasma}(z)}}\,. \tag{3.29}$$

In contrast to Ref. [55] which considered the case of sudden density transitions, we consider slow density downramps that cause the bubble to double in size over many bubble lengths, i.e., $n^{-1}dn/dz \ll 1$.

Fig. 3.5 shows the trajectory of a plasma electron that becomes trapped and accelerated by a growing bubble. Here, the model parameters are $\lambda_0 = 6$, $\sigma_z = 1.8$, and $\Delta_\rho = 0.4$. Fig. 3.5(a) shows the variation of the background plasma density along the propagation distance z: the initial density is $n_i = 1.2\, n_0$, and the linear downramp reduces the density to $n_f = n_0$ over a distance $L_{\rm ramp} = 40$. The bubble grows as a result of the density downramp as shown in Fig. 3.5(b): the solid black line is the initial bubble size, and the dashed black line is final bubble size. Such a density downramp gradient would cause this bubble to double in size over several tens of bubble lengths, so the bubble growth rate is very slow. The trajectory of the trapped electron, which has an impact parameter of $r_0 \approx 4.4$, is shown in red. Fig. 3.5(c) shows the Hamiltonian of the trapped electron in the frame co-moving with the bubble,

$$H = \sqrt{1 + (\mathbf{P} + \mathbf{A})^2} - v_0 P_z - \phi\,. \tag{3.30}$$

Interaction with the growing bubble, which is a deepening potential well, lowers the moving-frame Hamiltonian. Once the trapping condition [41] $H < 0$ is satisfied, the electron cannot leave the bubble and is accelerated by the fields inside the bubble.

As seen from the example trajectory in Fig. 3.5, electrons that become trapped and accelerated by the growing bubble approach the bubble from off-axis with an impact parameter $r_0 > 0$. It is for this reason that the wake-fields outside of the bubble are needed to accurately model the phenomenon of electron trapping. Fig. 3.6 shows the final moving-frame Hamiltonian of electrons versus the impact parameter from (a) the model and (b) the PIC code

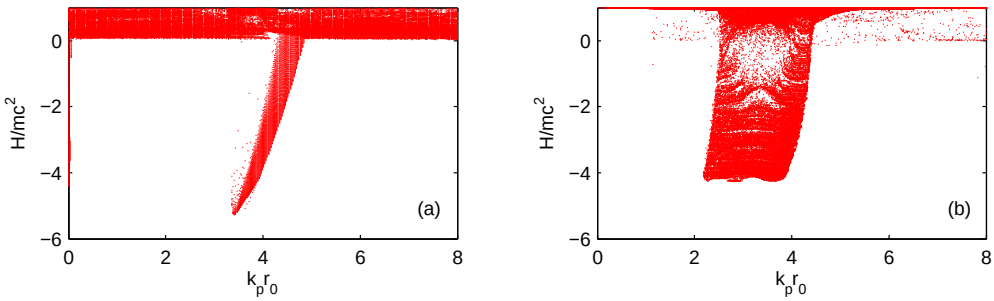

Figure 3.6: Final moving-frame Hamiltonian of electrons versus impact parameter from (a) the model and (b) WAKE. Here, $\lambda_0 = 6$, $\sigma_z = 1.8k_p^{-1}$, $\Delta_\rho = 0.4k_p^{-1}$, $\Delta_J = k_p^{-1}$, $n_i = 1.5n_0$, $n_f = n_0$, and $L_{\rm ramp} = 100k_p^{-1}$. Electrons with $H < 0$ are trapped.

WAKE, after interaction with the growing bubble. Here, $\lambda_0 = 6$, $\sigma_z = 1.8$, and $\Delta_\rho = 0.4$. The linear plasma downramp is given by $n_i = 1.5\ n_0$, $n_f = n_0$, and $L_{\rm ramp} = 100$. Again, the moving-frame Hamiltonian of electrons is reduced as a result of interaction with a growing bubble, and trapping occurs over a range of impact parameters $2 < r_0 < 5$. The range of impact parameters over which trapping occurs is greater in the PIC simulation than in the model. This is most likely due to the simplifying model assumptions that $\Delta_\rho = const$, $\Delta_J = const$. It is important to note here that the density downramps and hence bubble growth rates are the same in the model calculation as in the PIC simulation. Thus, with the new model presented here there is quantitative agreement on the bubble growth rate sufficient for trapping to occur.

Fig. 3.7 shows a comparison of the bubble expansion rates required for trapping in the idealized spherical bubble model (blue) and the more realistic model described in this chapter (red). In this figure, the bubble was allowed

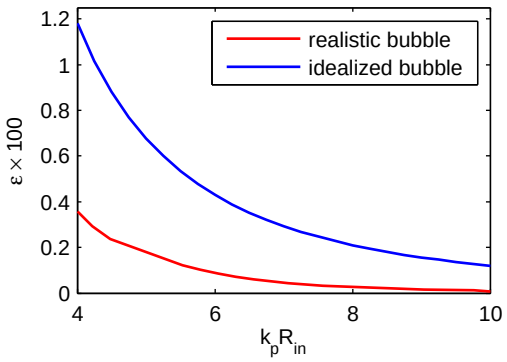

Figure 3.7: Comparison of bubble expansion rates required for trapping in the simplified spherical bubble model (blue) and the more realistic model described in this chapter (red). While the idealized spherical bubble model overestimates the expansion rate required for trapping, the new model agrees quantitatively with PIC simulation.

to expand according to $R(z) = R_{in}(1 + \epsilon z)$, where ϵ is the bubble expansion rate. The expansion rate ϵ may be related to the density gradient using Eq. (3.29). In both models the bubble had an ultrarelativistic velocity $v_0 = c$. The minimum value of ϵ which led to electron trapping as defined by the condition $H < 0$ is shown as a function of the initial bubble size. Although the expansion rate sufficient for trapping decreases with increasing bubble size it never becomes identically zero, consistent with the findings in Sec. 3.3.2. The simplified spherical bubble model overestimates the expansion rate required for trapping. In Chapter 2 this discrepancy was attributed to the role of the high density spike near the tail of the bubble. However, the inclusion of the electromagnetic fields surrounding the bubble into the model is in fact enough to give quantitative agreement with PIC simulation in the expansion rates required for trapping.

3.4 Summary

This chapter has presented an analytic model for plasma wakefield accelerators in the highly nonlinear bubble regime. In contrast to previous theories [29, 39], this model takes into account the detailed structure of the high density sheath and plasma return current outside of the bubble and gives accurate expressions for the electromagnetic fields in the regions surrounding the bubble. This is a significant improvement because these fields in the bubble exterior play a critical role in determining the behavior of electrons that become self-injected. This model has been used to study self-injection into an evolving bubble, and found to be in quantitative agreement with PIC simulations on the reduction of the electron moving-frame Hamiltonian sufficient for trapping [41]. The expansion rates required for trapping in ultrarelativistic bubbles have been characterized, and found to decrease for larger bubble sizes.

Chapter 4

Ionization induced injection

4.1 Injection due to field ionization by the drive pulse

The preceding chapters have focused on self-injection due to bubble evolution, where electrons become trapped by the dynamically deepening potential of an expanding bubble. This chapter will explore another injection method which is applicable to the blowout regime of plasma based accelerators, but does not require bubble evolution. First observed experimentally by Pak et al. [56], this injection technique involves doping the background gas (typically Helium) with an element of higher atomic number which possesses K shell electrons with a significantly higher ionization potential than the background gas. Referred to as ionization induced injection, it also requires the drive pulse to have a longitudinal profile such that the driver fields start out less intense in the front and ramp up to a higher intensity; a condition which is nearly always true. In this case, the electrons of the bulk gas as well as the outer shell electrons of the dopant are field ionized well ahead of bubble by the head of the drive pulse. In contrast, ionization of the inner shell dopant electrons occurs inside the bubble, where the drive pulse fields are higher and exceed the ionization threshold for these K shell electrons. These electrons are "born" inside the potential well of the bubble, with a negative Hamiltonian.

Thus, the electrons are trapped inside the bubble and become accelerated by the wakefields. The exact conditions under which electrons become trapped in this scenario were analyzed in Ref. [56], and will not be described beyond a qualitative way here.

Previous work [56, 57] demonstrating ionization induced injection utilized a laser driver focused to a spot size matched to the background plasma density, so that the drive pulse and bubble underwent minimal evolution during the course of the acceleration. Thus, the regions of maximum laser intensity stayed above the ionization threshold for the Nitrogen dopant used in the experiments. The result was continuous ionization induced injection over the propagation length, which lead to relatively broad electron energy spectra as electrons injected later experienced less energy gain than those injected earlier. The next section analyzes a scheme [58] for localized ionization induced injection, where evolution of the laser driver leads to termination of the injection process and results in narrower energy spreads. It will be shown that this effect was responsible for the quasimonoenergetic electron spectra observed in recent wakefield experiments performed at the Texas Petawatt facility. The effect of the choice of dopant gas species on the electron energy spreads will also be explored.

Table 4.1: Threshold ionization intensities estimated by the ADK model [59].

Ion species	a_0	Intensity at $\lambda = 1.053$ μm
N^{5+}	1.87	4.31×10^{18} W/cm^2
N^{6+}	2.47	7.53×10^{18} W/cm^2
O^{6+}	2.82	9.81×10^{18} W/cm^2
O^{7+}	3.58	1.58×10^{19} W/cm^2
F^{7+}	4.08	2.05×10^{19} W/cm^2

4.2 Controlled ionization injection due to laser driver evolution

4.2.1 Termination of ionization injection due to laser diffraction

The broad electron energy spectra observed in previous works [56, 57] was due to continuous ionization injection as a result of a matched laser driver propagating with a peak intensity always above the ionization threshold for the inner shell electrons. However, if a mismatched laser driver is allowed to evolve the peak intensity may drop below the ionization threshold during the later phases of acceleration, terminating the injection and producing beams of more narrow energy spread. Ideally, to maximize energy gain, a brief injection phase at the beginning of propagation is followed by an acceleration phase during which no further injection occurs. This is possible if the laser pulse is either focused, or relativistically self-focuses, to an intensity greater than the threshold for ionization of inner shell electrons, then defocuses during the course of its propagation.

Simulations performed to model the results of wakefield acceleration experiments carried out at the Texas Petawatt facility revealed that the scenario

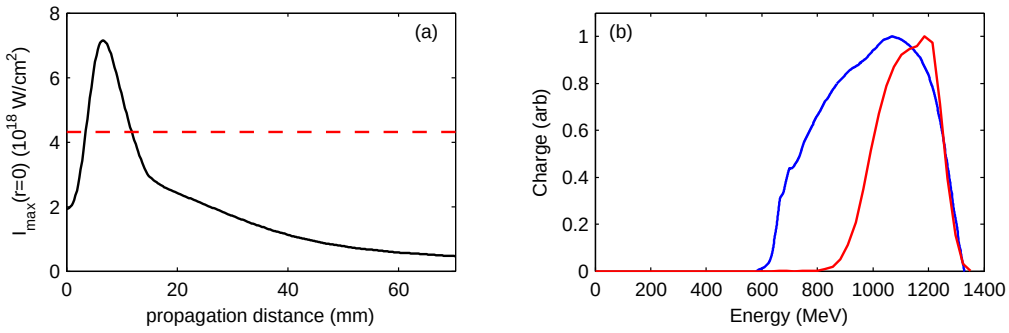

Figure 4.1: (a): Maximum laser intensity on axis as a function of propagation distance. The threshold ionization intensity for the N^{5+} ion is indicated with a red dashed line. Where the laser intensity is greater than the threshold intensity, ionization injection is expected to occur. (b): Experimental (blue) and simulated (red) electron energy spectra.

described above was responsible for the generation of quasi-monoenergetic electron beams with a central electron energy of approximately 1.2 GeV. To perform these simulations, the WAKE [42] code was upgraded with the capability to seed test electrons at a location where the laser intensity exceeds a threshold. Combined with estimates for the threshold ionization intensities given by the ADK model of tunnel ionization [59] as shown in Table 4.1, this allowed for accurate modeling of ionization induced injection and acceleration in the limit of low beam charge (i.e., negligible beam loading). It is worth noting here that although the ADK model does not take relativistic effects into account, experiments by Auguste et al [60] show that in practice it accurately predicts ionization thresholds for intensities on the order of 10^{18} W/cm^2.

Fig. 4.1 illustrates this effect as observed in the Texas Petawatt wakefield acceleration experiment. Fig. 4.1(a) shows the maximum laser intensity

on axis versus the propagation distance. The threshold ionization intensity for the N^{5+} ion of the Nitrogen dopant used in this experiment is indicated in dashed red. As seen in this figure, ionization induced injection is localized near the beginning of the interaction, and injection is clamped due to laser diffraction after approximately 15 mm. The simulation parameters in this case are as follows: $n_0 = 4 \times 10^{17}$ cm^{-3}, $a_0 = 1.25$, $w_0 = 50$ μm and $\tau_{\mathrm{FWHM}} = 150$ fs. These initial conditions were chosen after exhaustive parameter scanning to match the experimentally observed electron spectrum as shown in Fig. 4.1(b). These simulations reveal that the laser diffraction was due to an absence of a self-guided acceleration stage. The simulated drive pulse has an energy of approximately 15 J, compared to the experimentally measured laser amplifier output of 130 J. This indicates that the laser-plasma coupling efficiency was about 12%, which led to an initial self-focusing of the pump pulse followed by a gradual defocusing. Although bubble formation was briefly evident at the point of tightest laser self-focus where injection occurs, most of the acceleration was due to the mildly nonlinear wake excited by the diffracting pump. Self-injection of initially quiescent background electrons was not observed for these parameters, so that ionization induced injection was indeed the injection mechanism at work.

4.2.2 Effect of dopant species on electron spectra

The low laser-plasma coupling efficiency in the experiment modeled in Fig. 4.1 led to acceleration in the mildly nonlinear wake regime and subse-

quently a lower average electron energy than otherwise possible. To accelerate the ionization injected electrons to energies beyond that shown in Fig. 4.1(b), it is necessary access the self-guided blowout regime and take advantage of the higher accelerating gradients and extended acceleration distance offered by a plasma bubble. However, an important consideration here is the choice of dopant gas species, due to the different threshold ionization intensities for the inner shell electrons. Depending on the threshold intensity the ionization injection can be more or less localized, which can broaden or tighten the final electron energy spread. Moreover, the self-guided laser intensity may be above the ionization threshold for the K shell electrons of some elements resulting in continuous injection, while below the threshold for others making localized injection feasible.

The self-guided intensity may be estimated as follows. During the self-guided stage where diffraction is balanced by relativistic self-focusing, the matched spot size is estimated by [54]

$$k_p w_0 \approx 2\sqrt{a_0}\,, \tag{4.1}$$

while the power normalized to the critical power for relativistic self-focusing P_c is given by [61]

$$\frac{P}{P_c} = \frac{1}{32}(k_p w_0)^2 a_0^2\,. \tag{4.2}$$

Thus, the self-guided intensity is

$$a_0 \approx 2\left(\frac{P}{P_c}\right)^{\frac{1}{3}} \tag{4.3}$$

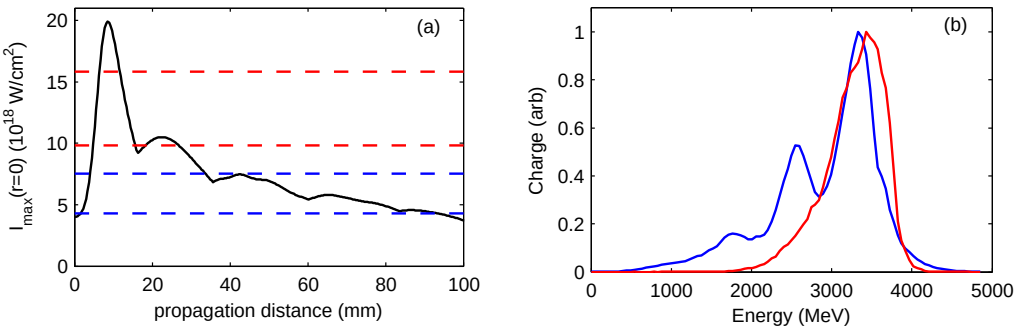

Figure 4.2: (a): Maximum laser intensity on axis as a function of propagation distance. The threshold ionization intensities for N^{5+} and N^{6+} are indicated by the blue dashed lines and O^{6+} and O^{7+} are indicated by the red dashed lines. Use of a Nitrogen dopant would lead to nearly continuous ionization injection in this case, while the use of Oxygen would result in a more localized burst of injection around the point of maximum self-focused intensity. (b): Electron spectra at 10 cm with a Nitrogen (blue) and Oxygen (red) dopant. The energy spread is narrower for the case of the Oxygen dopant due to more localized injection.

where $P/P_c > 1$ is required for relativistic self-focusing to occur. Hence, $a_0 \gtrsim 2$ for a self-guided pulse, and from Table 4.1 it is clear that a Nitrogen dopant will always lead to continuous ionization induced injection during any self-guided stage of laser propagation. This implies that for localized injection to occur and be clamped during the self-guided stage, a dopant gas with a greater threshold ionization intensity such as Oxygen must be considered.

Fig. 4.2(a) shows the maximum laser intensity on axis as a function of propagation distance for the parameters $n_0 = 3 \times 10^{17}$ cm^{-3}, $a_0 = 1.8$, $w_0 = 60$ μm and $\tau_{\mathrm{FWHM}} = 150$ fs. In this simulation the initially mismatched laser pulse relativistically self-focus to a maximum intensity of 2×10^{19} W/cm^2

before entering a self-guided stage at a lower intensity. Such laser dynamics is ideal for localized ionization injection near the beginning of the interaction, provided that an appropriate dopant gas is chosen. In Fig. 4.2(a) the threshold ionization intensities for the N^{5+} and N^{6+} ions are indicated by the blue dashed lines, showing that with a Nitrogen dopant ionization injection would be continuous. On the other hand, use of an Oxygen dopant would result in termination of the injection after the first 3 cm as indicated by the red dashed lines. Fig. 4.2(b) shows the accelerated electron spectra at the end of the plasma for a Nitrogen (blue) and an Oxygen (red) dopant. With a Nitrogen dopant the energy spectrum is broad because of the continuous injection throughout the length of the plasma. The energy spectrum given by an Oxygen dopant is narrower since ionization injection is localized to the beginning of the plasma.

4.3 Summary

This chapter has presented an alternative injection scheme, which relies on the K shell electrons of a dopant gas becoming field ionized by the driver inside the potential well of the bubble. Such electrons are trapped inside the bubble as soon as they are liberated from their atomic nuclei, so that this injection method does not necessitate bubble or driver evolution. However, without driver evolution electrons are injected into the bubble throughout the entire acceleration length, leading to broad electron beam spectra. With an evolving laser driver as well as the appropriate choice of dopant gas, narrower

energy spreads can nevertheless be achieved. Estimates for the self-guided laser intensity in the bubble regime indicate that a Nitrogen dopant will always lead to continuous ionization injection and the associated poor electron beam quality. Therefore, dopant gases of higher K shell ionization threshold intensities such as Oxygen should be considered for production of electron beams with high spectral quality.

Chapter 5

Frequency domain holographic imaging of plasma bubbles

5.1 Imaging plasma wakes

Experimentally imaging a plasma wake has the following issues: the plasma wake moves nearly at the speed of light, and the plasma wake structure are typically μm-scale. Thus, the wake cannot be measured through transverse imaging techniques in the lab frame, as the result of any such effort would be a blurred image. Frequency Domain Holography (FDH) [62] is an experimental technique that overcomes these problems, and produces snapshot images of plasma wakes. In this technique a probe laser pulse travels co-linearly, or almost co-linearly, with the plasma structure. The plasma index of refraction is given by

$$N = \sqrt{1 - \frac{\omega_p^2}{\omega_0^2}}\,, \tag{5.1}$$

where $\omega_p^2 = 4\pi e^2 n_e/m_e$ is the plasma frequency and ω_0 is the laser frequency. Variations in the refractive index due to the electron density perturbations of the plasma wake leave an imprint in the probe pulse in the form of a phase shift. Thus, the probe phase shift after the interaction gives a time-integrated measurement of the plasma density. FDH was first successfully applied to

image a linear regime plasma wake by Matlis *et al.* [63].

This chapter will give a brief review of the FDH technique, showing that it can be employed to extract the probe pulse phase shift and hence the density structure of a plasma wake traveling at relativistic velocity. A procedure for modeling of the probe pulse evolution and hologram formation will be described, and used to study the robustness of the probe reconstruction technique to experimental limitations such as finite bandwidth and refraction by the plasma wave. It will be shown that simulating the probe pulse propagation using the method of photon acceleration [64] gives localized probe frequency-shift information. Simulations of FDH with a slightly off-axis probe will be presented, showing that it is possible to experimentally measure the bubble evolution which leads to electron self-injection.

5.2 Frequency domain holography

To measure the density structure of the plasma wave to be imaged, the phase shift of the probe pulse must be obtained. Interferometry is used to extract the probe pulse phase shift; the probe is interfered with a reference pulse which is ahead of and does not interact with the wake. Interference is done in the frequency domain through the use of a spectrometer, to preserve resolution in the propagation direction z. The probe intensity $|E_{\mathrm{probe}}|^2$ and phase shift $\delta\phi(x,z)$ are then extracted from the interferogram through FFT post-processing. In practice, the probe and reference are frequency-doubled with respect to the pump laser pulse, if present, and a bandpass filter is used

to eliminate pump pulse noise from the FDH signal. The probe and reference pulses are chirped, so that they can be both temporally long enough to overlap with a significant portion of the wake, and have wide enough bandwidth to resolve temporally fine features of the wake.

5.2.1 Simulation of probe pulse evolution and frequency domain holography

The FDH technique can be simulated through the quasistatic PIC code WAKE [42]. WAKE calculates the evolution of chirped probe and reference pulses that are frequency-doubled with respect to the pump pulse, and outputs their complex amplitude $E(r,\xi)_{\mathrm{probe,\,ref}}$. The probe and reference pulses are assumed to be of low intensity; they evolve due to the nonlinear index of the plasma, but do not perturb the plasma. Taking the Fourier transform $E(r,\omega)_{\mathrm{probe,\,ref}}$, the simulated holograms can be calculated as

$$S_{\mathrm{FDH}}(r,\omega) = |E_{\mathrm{ref}}(r,\omega) + E_{\mathrm{probe}}(r,\omega)e^{i\omega\tau}|^2\,, \tag{5.2}$$

$$S_{\mathrm{vac}}(r,\omega) = |E_{\mathrm{ref}}(r,\omega) + E_{\mathrm{ref}}(r,\omega)e^{i\omega\tau}|^2\,, \tag{5.3}$$

where τ is the delay time between probe and reference. Examples of simulated holograms are shown in Fig. 5.1. The simulated FDH signals $S_{\mathrm{FDH,\,vac}}$ are windowed for a specified range of frequencies $\Delta\omega$ to simulate the finite bandwidth of the spectrometer, and the FDH reconstruction procedure is applied. By comparing the reconstructed intensity $|E_{\mathrm{probe}}|^2$ and phase shift $\delta\phi(r,z)$ to that directly extracted from the known complex probe amplitude, it is possible to analyze the effects of experimental limitations such as finite bandwidth and

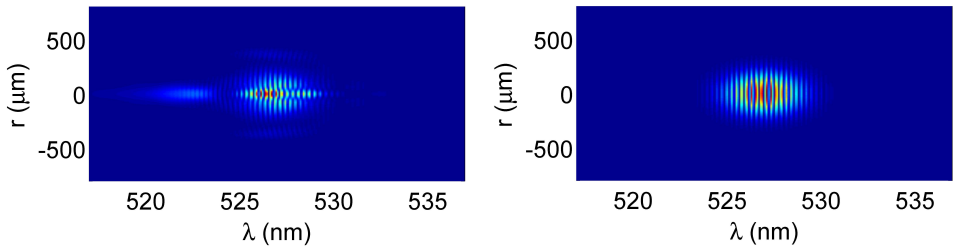

Figure 5.1: Example frequency domain holograms constructed from WAKE probe and reference pulse data. A hologram with fringe shifts due to interaction of the probe pulse with the plasma wake (left) and a null hologram with no shifts (right).

refraction by the plasma wave on the quality of the reconstruction. The results of such a study are presented in the next section.

5.3 Frequency domain holography in the bubble regime

5.3.1 Refraction by the plasma bubble and formation of optical bullets

Simulations and modeling of the FDH technique were crucial to the interpretation of experimental data in Dong *et al* [65]. The goal of this experiment was to extend to application of FDH to the highly nonlinear bubble regime of LWFA. In this experiment plasma bubbles were created using the HERCULES laser at the University of Michigan, which produced 30 TW, 30 fs FWHM pulses with a central wavelength 800 nm that were focused to a spot size of 10 μm. When these pulses were focused onto a 2 mm Helium gas jet with plasma density $10^{19} \lesssim n_e \lesssim 3 \times 10^{19}$ cm^{-3}, accelerated electrons were

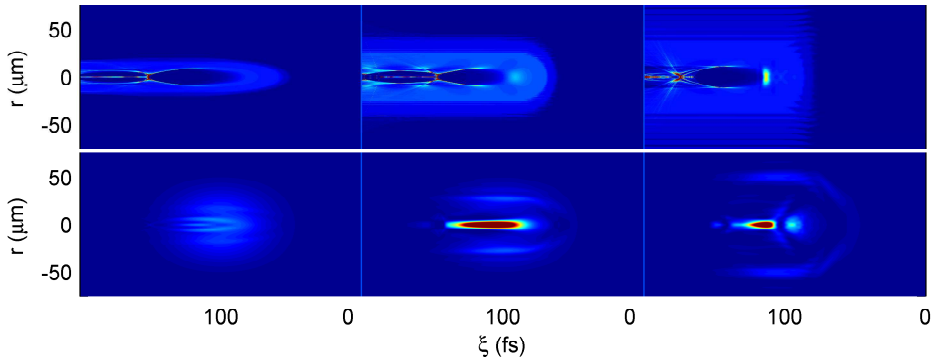

Figure 5.2: (top row): WAKE simulations showing formation of the plasma bubble. (2nd row): refraction of the probe pulse to form an optical bullet inside the bubble. Here, the left column is at the plasma entrance $z = 0.1$ mm, middle column at propagation distance $z = 0.5$ mm, and the right column at plasma exit $z = 1.8$ mm.

observed at the higher ranges of density. The FDH technique was applied to image the plasma bubbles experimentally.

Initial experimental FDH results showed that the phase shift $\delta\phi(r, z)$ was very large, due to the highly nonlinear wake, making phase unwrapping unreliable. Furthermore, bright spots were observed in the reconstructed probe intensity $|E_{\text{probe}}|^2$, a feature not seen in the linear wake regime. Simulations revealed that these bright spots were formed by the focusing effect of a plasma bubble, and that these optical "bullets" were a signature of bubble formation.

Fig. 5.2 shows a WAKE simulation for the density $n_e = 0.8 \times 10^{19}$ cm^{-3}. The top row shows pseudocolor plots of the plasma density; illustrating the formation and evolution of the plasma bubble. The second row shows the refraction of the probe pulse light due to the nonlinear plasma index varia-

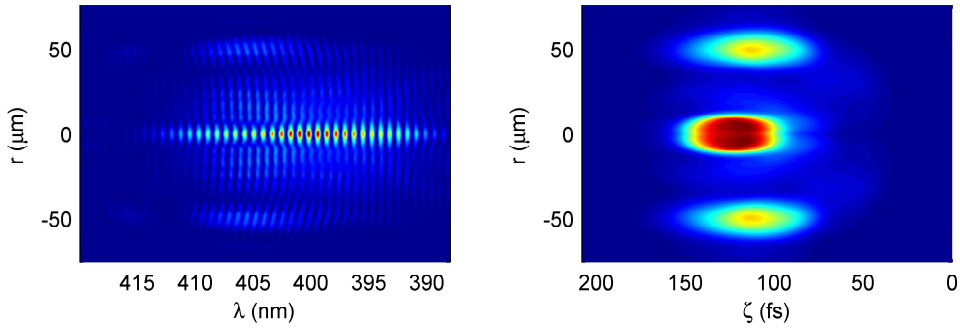

Figure 5.3: (left): Simulated frequency domain hologram showing a broadened streak at $r = 0$ corresponding to bullet inside the bubble. (right): probe intensity profile reconstructed from simulated frequency domain hologram using experimental spectrometer bandwidth and resolution.

tion, with the formation of an optical bullet can be clearly evident. Fig. 5.3 shows a simulated frequency domain hologram and its reconstructed probe intensity. Reconstruction of the simulated hologram confirmed that while the probe phase shift became very large due to the highly nonlinear wake and was further scrambled in the transverse direction due to the refraction of the plasma bubble, the optical bullet feature could nevertheless be recovered.

5.3.2 Effects of finite spectrometer bandwidth

As seen in the previous subsection, the formation of a short tightly focused optical bullet is a characteristic signature of the bubble regime. This short bullet is manifested as a spectrally broad feature in the frequency domain hologram as seen in Fig. 5.3. Thus, the hologram must preserve enough spectral information to reconstruct the bullet feature accurately, and clipping

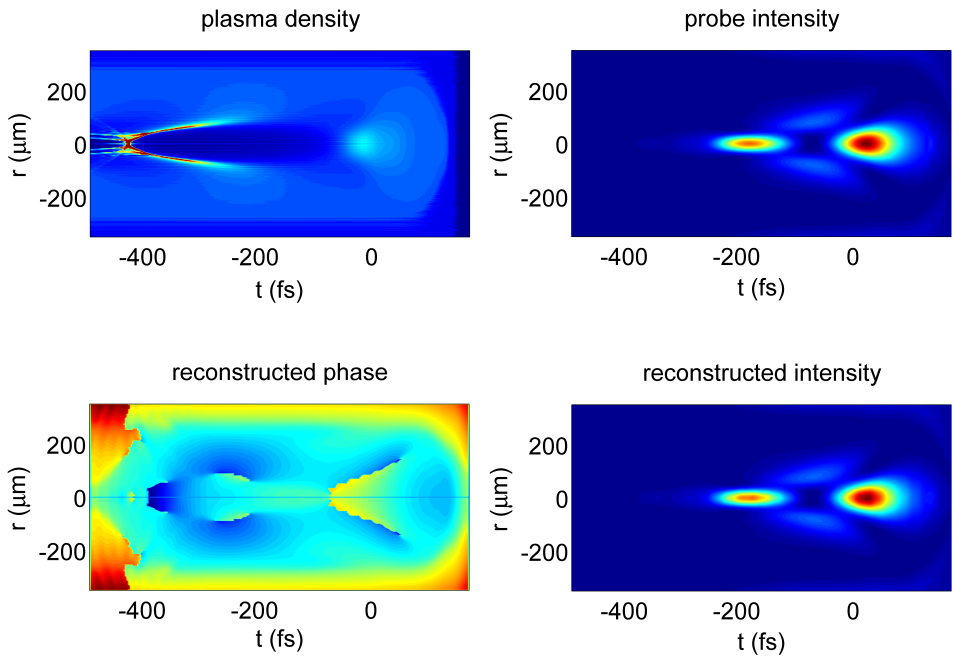

Figure 5.4: Top row: WAKE simulation data with plasma density (left) and probe pulse intensity (right) for the parameters of the Texas Petawatt experiment with a coaxial probe. The probe pulse is focused into an optical bullet due to interaction with the plasma bubble. Bottom row: reconstructions of probe pulse phase (left) and intensity (right) from the simulated frequency domain hologram. Here, the spectrometer is assumed to have a bandwidth $\Delta\lambda = 70$ nm centered around $\lambda = 535$ nm.

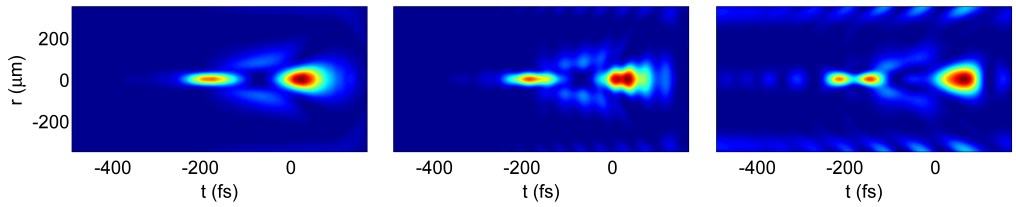

Figure 5.5: Reconstructions of probe intensity, with same parameters as in Fig. 5.4, and spectrometer bandwidth 500−570 nm (left) 507−547 nm (center) and 517 − 537 nm (right). The quality of the reconstruction degrades as spectrometer bandwidth decreases.

of the spectral data may lead to degradation of the reconstruction quality. It is therefore of interest how much spectral bandwidth must be measured in order to insure that the reconstruction procedure is successful. Here, modeling of the ongoing experimental efforts to use FDH to image plasma bubbles at the Texas Petawatt laser facility is of particular interest.

Fig. 5.4 shows simulation data for the plasma bubble and resulting optical bullet (top row), and the corresponding simulated FDH reconstructions of probe phase and intensity (bottom row). Here, the plasma density is $n_e = 10^{17}$ cm^{-3}, the plasma length is 8 cm, and the pump laser parameters are the ideal parameters of the Texas Petawatt (200 J, 150 fs, $w_0 = 80$ μm). Since the pump in this case has a central wavelength 1053 nm, the frequency doubled probe and reference have 527 nm. The probe-reference delay is taken to be $\tau = 3.5$ ps, and are chirped so that they initially have approximately 8 nm of bandwidth. Reconstructions of simulated FD holograms show that good reconstructions of probe phase shift and intensity are possible in the case where the spectrometer has a bandwidth $\Delta\lambda = 70$ nm. However, the

quality of reconstructions degrade for narrower spectrometer bandwidths as seen in Fig. 5.5. Although the main optical bullet feature remains resolvable distortions in the intensity reconstruction are evident, and the phase is again unrecoverable for the more narrow bandwidths. It should be noted that these artifacts become more severe with increasing electron density, where there plasma refractive index gradients increase.

5.3.3 Simulation of probe pulse evolution using the photon acceleration technique

The PIC code WAKE simulates the evolution of the probe pulse by numerically solving the paraxial wave equation, taking into account the nonlinear plasma index calculated from quasistatic particles. An alternative way to model the probe pulse evolution is to use the method of photon acceleration [64]. Here, the probe is modeled as a collection of individual photons, and their trajectories are calculated from the Hamiltonian equations of motion while using the plasma density perturbations obtained from WAKE.

From the plasma dispersion relation, the photon Hamiltonian (normalized to $\hbar$) is (Mendonça [64], Eq. 2.12)

$$\omega(\vec{r},\vec{k}) = \sqrt{\omega_p^2(\vec{r}) + c^2k^2}\,, \tag{5.4}$$

where $\omega_p^2(\vec{r}) = 4\pi e^2 n_e(\vec{r})/m_e$ is the plasma frequency, $\vec{r}$ is the location vector, and the photon momentum is $\vec{p} = c\vec{k}$. The equations of motion are then given

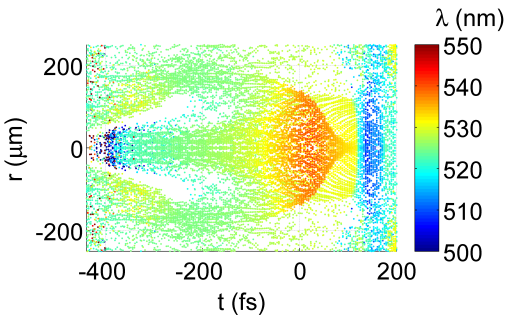

Figure 5.6: Location of probe pulse photons $z = 8$ cm into plasma. Photons have been colored to indicate their shift from an initial average wavelength of $\lambda_0 = 527$ nm.

by

$$\frac{d\vec{r}}{dt} = \frac{\partial\omega}{\partial\vec{k}} = \frac{c^2\vec{k}}{\omega}\,, \tag{5.5}$$

$$\frac{d\vec{k}}{dt} = -\frac{\partial\omega}{\partial\vec{r}} = -\frac{1}{\omega}\frac{\partial\omega_p^2}{\partial\vec{r}}\,. \tag{5.6}$$

The total variation of the photon phase is given by $d\phi = \vec{k}\cdot\vec{r} - \omega dt$ (Mendonça [64], Eq. 2.64), so that the equation of motion for the photon phase is

$$\frac{d\phi}{dt} = \vec{k}\cdot\frac{d\vec{r}}{dt} - \omega = \frac{c^2k^2}{\omega} - \omega\,. \tag{5.7}$$

Numerical integration of Eqs. (5.5)-(5.7) gives the trajectories and phase shift of each photon. The probe pulse field is then calculated by interpolating the complex amplitude of each photon $e^{i\phi}$ to a grid.

There are several advantages to modeling the probe pulse evolution using the photon acceleration technique. First, by keeping track of the phase evolution of each photon localized information about the probe frequency-shift

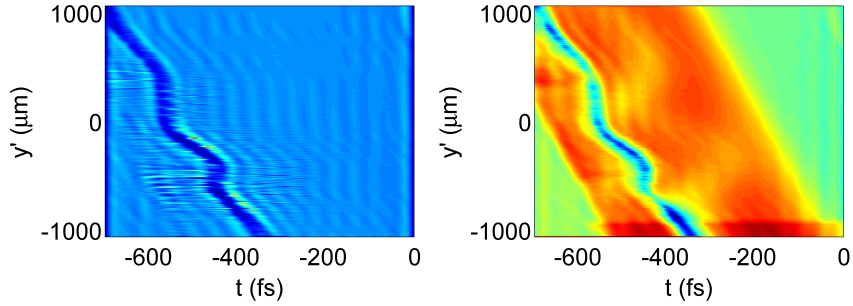

Figure 5.7: Reconstructed probe pulse intensity (left) and phase (right) from off-axis interaction between probe and plasma bubble. Here, the probe and pump pulses propagate at a relative angle $\theta = 4.5°$, and plots are in the probe pulse coordinates. The bubble travels across the probe pulse from bottom right to upper left. In the phase shift plot, going from right to left, the first line represents the path of the ionization front, and the second curved line is the imprint left by the density spike at the tail of the evolving plasma bubble.

can be obtained. Fig. 5.6 shows the results of a photon swarm simulation, for the same parameters as in Fig. 5.4. The location of probe pulse photons at $z = 8$ cm is shown, with each photon colored to indicate its frequency shift. The photons are not initially monochromatic because the probe pulse is chirped, but have the average initial wavelength $\lambda_0 = 527$ cm.

The probe and reference pulse in WAKE necessarily propagate coaxially with respect to the pump due to the assumption of azimuthal symmetry. Thus, a second advantage of the photon acceleration technique is the new ability to model probe pulses that propagate off-axis with respect to the pump. The result of a photon swarm simulation is shown in Fig. 5.7, where the probe pulse propagates at a relative angle $\theta = 4.5°$ with respect to the pump. Fig. 5.7 is

in the probe pulse coordinates, where rotation in the $y - z$ plane is given by

$$z' = z\cos\theta + y\sin\theta\,, \tag{5.8}$$

$$y' = -z\sin\theta + y\cos\theta\,, \tag{5.9}$$

and shows the reconstruction of the probe pulse intensity (left) and phase shift (right). Physical parameters are the same as in Fig. 5.6, except for the plasma density which is increased to $n_e = 2.5 \times 10^{17}$ cm^{-3}.

In contrast with the coaxial probe, simulations show that in the off-axis case the probe phase shift is relatively small, allowing for unwrapping of the reconstructed phase. Furthermore, Fig. 5.7 shows that the density spike at the tail of the plasma bubble leaves a distinct imprint in both the probe intensity and phase, and that the time evolution of the bubble size can thus be measured. It has been shown in the previous chapters that evolution of the plasma bubble plays a crucial role in the self-injection of background plasma electrons [41], and the simulations presented above indicate that the off-axis FDH technique may provide a direct experimental verification of this important injection mechanism.

5.4 Summary

This chapter has described two techniques for modeling of the probe pulse evolution: the WAKE code and the method of photon acceleration. It has been shown that frequency domain holograms can be constructed from the simulation data, and used to study the robustness of the FDH recon-

struction technique to experimental limitations such as finite bandwidth and refraction by the plasma wave. In co-axial geometry where interaction between the probe and bubble is very strong, it is important to measure enough spectral bandwidth in order to insure accurate reconstruction phase and intensity. Simulations of FDH with a slightly off-axis probe show that it is possible to experimentally measure the bubble evolution which leads to electron self-injection.

Chapter 6

Conclusion

Plasma based accelerators offer high gradient, compact generation of relativistic electron beams. Modern wakefield accelerators operate in the bubble regime due to the narrower electron spectra, an important measure of beam quality. This thesis has presented a theoretical and computational analysis of the injection mechanisms used in bubble regime wakefield accelerators.

Using an idealized spherical model of the plasma bubble it was shown that an expanding bubble can trap electrons by acting as a dynamically deepening potential well. A sufficient condition for trapping was derived and the expansion rates sufficient for trapping characterized as a function of the bubble Lorentz factor. This is significant for laser driven accelerators because the bubble speed is determined by the pump pulse group velocity, which is in turn given by the plasma density. For rarefied plasmas which give the longest dephasing length and greatest energy gain the bubble is highly relativistic with a large Lorentz factor, and it was shown using the idealized model and PIC simulations that bubble expansion is necessary for self-injection to occur in this regime.

Trapping by an expanding bubble was further analyzed in the context

of ultrarelativistic electron beam driven bubbles. A realistic model of the beam driven bubble was derived which takes into account the detailed charge and current distribution in the regions immediately surrounding the bubble. The electromagnetic fields outside the bubble were shown to determine the trapping dynamics, and critical expansion rates for trapping were characterized as a function of the bubble size. These threshold rates were in turn related to the background plasma density gradients that lead to self-injection.

An alternative injection mechanism due to field ionization of gas ions inside the bubble was studied using a novel PIC simulation technique. A method for generation of quasimonoenergetic electron beams using this injection scheme was analyzed, and the effects of dopant gas species and laser driver evolution on the electron beam quality were studied. Estimates for the self-guided pump intensity in the bubble regime indicate that the commonly used Nitrogen dopant will lead to broad electron spectra for laser drivers at optical wavelengths, so that dopant gases of higher atomic numbers (and hence greater K shell ionization threshold intensities) should be considered.

Lastly, frequency domain holographic imaging of bubble regime wakefield accelerators was analyzed using PIC simulations and the method of photon acceleration. Modeling of the probe beam interaction with a bubble showed that it is possible to apply the FDH technique to measure the bubble evolution which leads to electron self-injection.

Bibliography

[1] L. Tonks and I. Langmuir. *Phys. Rev.*, **33**:195, 1929.

[2] T. Tajima and J. M. Dawson. *Phys. Rev. Lett.*, **43**:267, 1979.

[3] W. P. Leemans, B. Nagler, and A. J. Gonsalves *et al.* *Nature Phys.*, **2**:696, 2006.

[4] S. Karsch, J. Osterhoff, and A. Popp *et al.* *Nature Phys.*, **9**:415, 2007.

[5] N. A. Hafz, T. M. Jeong, and I. Choi *et al.* *Nature Photonics*, **2**:571, 2008.

[6] J. Osterhoff, A. Popp, and Zs. Major *et al.* *Phys. Rev. Lett.*, **101**:085002, 2008.

[7] S. Kneip, S. R. Nagel, and S. F. Martins *et al.* *Phys. Rev. Lett.*, **103**:035002, 2009.

[8] I. Blumenfeld *et al.* *Nature*, **445**:741, 2007.

[9] B. K. Vainshtein. *Acta Crystallogr. B*, **47**:145, 1991.

[10] A. Caldwell *et al.* *Nat. Phys.*, **5**:363, 2009.

[11] C. B. Schroeder, E. Esarey, C. G. R. Geddes, C. Benedetti, and W. P. Leemans. *Phys. Rev. ST Accel. Beams*, **13**:101301, 2010.

[12] K. R. Hogstrom and P. R. Almond. *Phys. Med. Biol.*, **51**:R455, 2006.

[13] D. Doria, K. F. Kakolee, S. Kar, S. K. Litt, F. Fiorini, H. Ahmed, S. Green, J. C. G. Jeynes, J. Kavanagh, D. Kirby, K. J. Kirkby, C. L. Lewis, M. J. Merchant, G. Nersisyan, R. Prasad, K. M. Prise, G. Schettino, M. Zepf, and M. Borghesi. *AIP Advances*, **2**:011209, 2012.

[14] P. Maine, D. Strickland, P. Bado, M. Pessot, and G. Mourou. *IEEE J. Quantum Electron.*, **QE-24**:398, 1988.

[15] M. N. Rosenbluth and C. S. Liu. *Phys. Rev. Lett.*, **29**:701, 1972.

[16] C. E. Clayton, C. Joshi, C. Darrow, and D. Umstadter. *Phys. Rev. Lett.*, **54**:2343, 1985.

[17] Y. Kitagawa, T. Matsumoto, T. Minamihata, K. Sawai, K. Matsuo, K. Mima, K. Nishihara, H. Azechi, K. A. Tanaka, H. Takabe, and S. Nakai. *Phys. Rev. Lett.*, **68**:48, 1992.

[18] C. E. Clayton, K. A. Marsh, A. Dyson, M. Everett, A. Lal, W. P. Leemans, R. Williams, and C. Joshi. *Phys. Rev. Lett.*, **70**:37, 1993.

[19] N. E. Andreev, L. M. Gorbunov, V. I. Kirsanov, A. A. Pogosova, and R. R. Ramazashvili. *Pis'ma Zh. Eksp. Teor. Fiz.*, **55**:551, 1992.

[20] Jr. T. M. Antonsen and P. Mora. *Phys. Rev. Lett.*, **69**:2204, 1992.

[21] G. Z. Sun, E. Ott, Y. C. Lee, and P. Guzdar. *Phys. Fluids*, **30**:526, 1987.

[22] K. Nakajima, D. Fisher, T. Kawakubo, H. Nakanishi, A. Ogata, Y. Kato, Y. Kitagawa, R. Kodama, K. Mima, H. Shiraga, K. Suzuki, K. Yamakawa, T. Zhang, Y. Sakawa, T. Shoji, Y. Nishida, N. Yugami, M. Downer, and T. Tajima. *Phys. Rev. Lett.*, **74**:4428, 1995.

[23] C. A. Coverdale, C. B. Darrow, C. D. Decker, W. B. Mori, K-C. Tzeng, K. A. Marsh, C. E. Clayton, and C. Joshi. *Phys. Rev. Lett.*, **74**:4659, 1995.

[24] A. Modena, Z. Najmudin, A. E. Dangor, C. E. Clayton, K. A. Marsh, C. Joshi, V. Malka, C. B. Darrow, C. Danson, D. Neely, and F. N. Walsh. *Nature*, **377**:606, 1995.

[25] A. Pukhov and J. Meyer ter Vehn. *Appl. Phys. B*, **74**:355, 2002.

[26] S. P. D. Mangles, C. D. Murphy, and Z. Najmudin *et al.* *Nature*, **431**:535, 2004.

[27] C. G. D. Geddes, Cs. Toth, and J. van Tilborg *et al.* *Nature*, **431**:538, 2004.

[28] J. Faure, Y. Glinec, and A. Pukhov *et al.* *Nature*, **431**:541, 2004.

[29] I. Kostyukov, A. Pukhov, and S. Kiselev. *Phys. Plasmas*, **11**:5256, 2004.

[30] J. M. Dawson. *Phys. Rev. Lett.*, **113**:383, 1959.

[31] Claire Ellen Max, Jonathan Arons, and A. Bruce Langdon. *Phys. Rev. Lett.*, **33**:209, 1974.

[32] B. Hafizi, A. Ting, P. Sprangle, and R. F. Hubbard. *Phys. Rev. E*, **62**:4120, 2000.

[33] W. L. Kruer. *The Physics of Laser Plasma Interactions.* Addison-Wesley, Redwood City, 1988.

[34] E. Esarey, P. Sprangle, J. Krall, and A. Ting. *Plasma Science, IEEE Transactions on*, **24**:252, 1996.

[35] Pisin Chen, J. M. Dawson, Robert W. Huff, and T. Katsouleas. *Phys. Rev. Lett.*, **54**:693, 1985.

[36] J. J. Su, T. Katsouleas, J. M. Dawson, P. Chen, M. Jones, and R. Keinigs. Stability of the driving bunch in the plasma wakefield accelerator. *Plasma Science, IEEE Transactions on*, **15**:192, 1987.

[37] K. L. F. Bane, P. Chen, and P. B. Wilson. *IEEE Transactions on Nuclear Sci.*, **NS-32**:3524, 1985.

[38] J. B. Rosenzweig, B. N. Breizman, T. Katsouleas, and *et al. Phys. Rev. A*, **44**:R6189, 1991.

[39] W. Lu, C. Huang, M. Zhou, W. B. Mori, and T. Katsouleas *et al. Phys. Rev. Lett.*, **96**:165002, 2006.

[40] I. Kostyukov, E. Nerush, A. Pukhov, and V. Seredov. *Phys. Rev. Lett.*, **103**:175003, 2009.

[41] S. Kalmykov, S. A. Yi, V. Khudik, and G. Shvets. *Phys. Rev. Lett.*, **103**:135004, 2009.

[42] P. Mora and Jr. T. M. Antonsen. *Phys. Plasmas*, **4**:217, 1997.

[43] D. L. Bruhwiler and J. R. Cary. *Phys. Rev. Lett.*, **68**:255, 1992.

[44] L. P. Pitaevskii and E. M. Lifshitz. *Physical Kinetics*. Pergamon Press, Oxford, 1981.

[45] S. Wilks, T. Katsouleas, J. M. Dawson, P. Chen, and J. J. Su. Beam loading in plasma waves. *Plasma Science, IEEE Transactions on*, **15**:210, 1987.

[46] M. Tzoufras *et al. Phys. Rev. Lett.*, **101**:145002, 2008.

[47] M. Tzoufras, W. Lu, and F. S. Tsung *et al. Phys. Plasmas*, **16**:056705, 2009.

[48] M. Martinez, E. Gaul, and T. Ditmire *et al. Proc. of SPIE*, **5991**:59911N, 2006.

[49] W. Lu *et al. Phys. Plasmas*, **13**:056709, 2006.

[50] S. A. Yi *et al. Plasma Phys. Control. Fusion*, **53**:014012, 2011.

[51] P. Sprangle *et al. Phys. Rev. Lett.*, **64**:2011, 1990.

[52] R. Keinigs *et al. Phys. Fluids*, **30**:252, 1987.

[53] D. H. Whittum *et al. Phys. Rev. Lett.*, **67**:991, 1991.

[54] W. Lu, M. Tzoufras, C. Joshi, F. S. Tsung, W. B. Mori, J. Vieira, R. A. Fonseca, and L. O. Silva. *Phys. Rev. ST Accel. Beams*, **10**:061301, 2007.

[55] H. Suk *et al. Phys. Rev. Lett.*, **86**:1011, 2001.

[56] A. Pak *et al. Phys. Rev. Lett.*, **104**:025003, 2010.

[57] C. E. Clayton, J. E. Ralph, F. Albert, R. A. Fonseca, S. H. Glenzer, C. Joshi, W. Lu, K. A. Marsh, S. F. Martins, W. B. Mori, A. Pak, F. S. Tsung, B. B. Pollock, J. S. Ross, L. O. Silva, and D. H. Froula. *Phys. Rev. Lett.*, **105**:105003, 2010.

[58] K. A. Marsh, C. E. Clayton, C. Joshi, W. Lu, W. B. Mori, A. Pak, and L. O. Silva. *Proceedings of the Particle Accelerator Conference*, page 707, 2011.

[59] M. V. Ammosov, N. B. Delone, and V. P. Krainov. *Sov. Phys. JETP*, **64**:1191, 1986.

[60] T. Auguste, P. Monot, L. A. Lompre, G. Mainfray, and C. Manus. *J. Phys. B*, **25**:4181, 1992.

[61] P. Sprangle, Cha-Mei Tang, and E. Esarey. Relativistic self-focusing of short-pulse radiation beams in plasmas. *Plasma Science, IEEE Transactions on*, **15**:145, 1987.

[62] S. P. Le Blanc, E. W. Gaul, N. H. Matlis, A. Rundquist, and M. C. Downer. *Opt. Lett.*, **25**:764, 2000.

[63] N. Matlis *et al.* *Nature Phys.*, **2**:749, 2006.

[64] J. T. Mendonça. *Theory of Photon Acceleration.* Bristol: IOP, 2001.

[65] P. Dong *et al.* *Phys. Rev. Lett.*, **104**:134801, 2010.